J. Fluid Mech. (2005), *vol.* 528, *pp.* 135–172.
doi:10.1017/S0022112004003210 Printed in the United Kingdom

Scalar mixing from a concentrated source in turbulent channel flow

By R. A. LAVERTU AND L. MYDLARSKI

Department of Mechanical Engineering, McGill University, 817 Sherbrooke Street West, Montréal, QC, H3A-2K6, Canada

(Received 7 October 2003 and in revised form 20 October 2004)

The mixing of a scalar (temperature) emitted from a concentrated line source in fully developed high-aspect-ratio turbulent channel flow is studied. The motivation for the work is to study the effect of the inhomogeneity on the scalar dispersion. It is most readily carried out in a flow that is inhomogeneous in only one direction, i.e. channel flow. Experiments were performed at two Reynolds numbers ($Re \equiv \langle U(y = h)\rangle h/\nu = 10\,400$ and $22\,800$), three wall-normal source locations ($y_s/h = 0.067$, 0.17 and 1.0) and six downstream distances ($4.0 \leqslant x/h \leqslant 22.0$). Both the mean and r.m.s. temperature profiles were found to be described well by truncated Gaussian distributions. In contrast to homogeneous flows, (i) the growth rates of the mean profile widths did not exhibit power law behaviours, (ii) the centres of the r.m.s. profiles were found to drift towards the centre of the channel for plumes emanating from off-centreline source locations and (iii) the r.m.s. profiles showed no tendency towards double peaks far downstream, as are observed in homogeneous flows. For near-wall source locations, the probability density function (PDF) of the scalar fluctuations evolved from a quasi-Gaussian distribution near the wall to a strongly positively skewed PDF (with a large spike at the cold-fluid temperature) for transverse locations away from the wall. Increasing the Reynolds number was found to improve the mixing, even though this decreases the amount of time for which the scalar can mix (owing to the more rapid advection). For the centreline source location, the PDF shape was, in general, more spiked, indicating the importance of the flapping of the plume in this case. The effect of the meandering of the plume was less significant when the plume was bounded by the wall. Second- and third-order velocity–temperature correlations were presented. The differences in their profiles for the near-wall and centreline source locations were distinct.

1. Introduction

The diffusion of scalars (e.g. temperature, mass, etc.) in turbulent flows is relevant to a variety of scientific and engineering phenomena, including heat transfer, combustion, meteorology, oceanic science and environmental pollutant dispersion. To model and predict such processes accurately, a thorough understanding of scalar mixing in a turbulent fluid is therefore required. Reviews of the subject have been compiled by Sreenivasan (1991), Shraiman & Siggia (2000) and Warhaft (2000).

A problem of particular interest is the diffusion of scalars from concentrated sources in turbulent flows. A classic example is the dispersion of a contaminant from a smokestack in the atmospheric boundary layer. Here, a scalar (the contaminant) is injected into the turbulent surroundings at a scale much smaller than the integral scale of the velocity field. Consequently, the plume emitted by the smokestack – initially of

a characteristic size of the same order as the smokestack exit diameter – grows as it is transported downstream. Experiments, simulations and theoretical work have been devoted to furthering our understanding of problems of this nature.

The most fundamental problem is scalar dispersion from a concentrated source in the simplest turbulent flow: homogeneous, isotropic turbulence. Though basic in principle, its details are nevertheless complex. The difficulties increase when considering scalar mixing from a concentrated source in homogeneous, but anisotropic, turbulent shear flow. (A thorough literature review of these two subjects is given in Karnik & Tavoularis 1989.) The complexity further increases when the problem is extended to inhomogeneous flows. Some of the previous work is summarized herein.

Taylor's (1921) work inspired experiments studying the mean and fluctuating temperature field downstream of a line source in (homogeneous, isotropic) grid-generated turbulence. Among the first were Taylor (1935), Uberoi & Corrsin (1953) and Townsend (1954). Subsequent work showed that the (time-averaged) mean temperature profiles are Gaussian and that the development of the thermal plume in this flow can be divided into three stages: molecular diffusive, turbulent convective and turbulent diffusive. In the molecular-diffusive range ($t \ll \kappa/\langle v^2 \rangle$), the growth of the mean temperature profile width, σ_{mean}, (where σ is the standard deviation of a Gaussian profile – a measure of its width) increases as $t^{1/2}$. (t is the diffusion time, κ is the thermal diffusivity and $\langle v^2 \rangle$ is the velocity variance in the transverse direction.) In the turbulent–convective range ($\kappa/\langle v^2 \rangle \ll t \ll \tau_L$, where τ_L is the Lagrangian integral time-scale), the spreading of σ_{mean} increases linearly with time. In the final stage, where $t \gg \tau_L$, the spreading is proportional to $t^{(2-n)/2}$, where n is the decay exponent of the velocity field and takes on values close to one (Stapountzis *et al.* 1986). Though the mean temperature profiles are Gaussian, the r.m.s. profiles of the temperature fluctuation are non-Gaussian (Warhaft 1984; Stapountzis *et al.* 1986). The effect of downstream distance of the wire from the grid on the mean and r.m.s. profiles was also studied by Warhaft (1984).

Stapountzis *et al.* (1986) compared their experimental results of scalar dispersion in homogeneous isotropic turbulence with the Lagrangian stochastic model of Sawford & Hunt (1986). (See also Durbin 1980 and Thomson 1990.) They found that molecular diffusion and viscosity affect the development of the thermal plume – particularly the intensity of the temperature fluctuations – in all stages, not just in the molecular-diffusive range. Anand & Pope (1983) also numerically studied scalar dispersion in this flow. They developed a quantitative relation for all three stages of development of the thermal plume using probability density function (PDF) methods. Livescu, Jaberi & Madnia (2000) employed direct numerical simulation to study dispersion from a single line source in homogeneous isotropic turbulence.

A line source placed in a homogeneous turbulent shear flow will determine the effect of shear (an anisotropy) on the scalar dispersion. Detailed measurements of the resultant thermal plume in such a flow field have been undertaken by Stapountzis & Britter (1987), Karnik & Tavoularis (1989) and Chung & Kyong (1989). The mean and r.m.s. temperature profiles have been documented in detail. Additionally, quantities such as velocity–temperature correlations, temperature PDFs, and joint velocity–temperature PDFs were compiled. Numerical simulations of similar experiments have been performed by Wilson, Flesch & Swaters (1993) and Cho & Chung (1997).

The subject of the present work is scalar dispersion from a concentrated source in inhomogeneous turbulent channel flow. The flow is fully developed and the channel has a high aspect ratio. Consequently, it is inhomogeneous in only the wall-normal direction. Scalar mixing from concentrated sources has been studied in other

inhomogeneous flows – predominantly boundary layers and jets, which are inhomogeneous in a minimum of two directions. Because most 'practical' flows are inhomogeneous, it is desirable to determine explicitly the effect of the inhomogeneity on the dispersion of the scalar by studying it in a fully developed duct flow. This motivates the present work, where it will be shown that the scalar mixing process varies strongly from the wall to the channel centreline. In addition to elucidating the effect of the inhomogeneity, the results presented herein will serve as a reference for numerical simulations of turbulence. This is particularly true given that channel flows more readily lend themselves to numerical simulation than boundary-layer flows. Nevertheless, the previous work on scalar mixing from concentrated sources in turbulent boundary layers is of interest. Motivated by the need to further understand atmospheric pollutant dispersion, the thermal plume behind a line source in a turbulent boundary layer has received significant attention.

Over a narrow range in both the streamwise direction (such that this direction can be effectively considered homogeneous) and the wall-normal directions, some results in boundary-layer flow may be similar to those in fully developed channel flow. Specifically, for (i) small downstream distances and (ii) source locations and plumes contained entirely in the inner layer (generally $y/h < 0.1$ (Pope 2000)), the velocity fields of the two flows and the consequent scalar dispersion should be similar. However, because the geometry of channel flow is significantly different from that of boundary-layer flow, should (i) the plume have dispersed far enough downstream such that the inhomogeneity in this direction can no longer be neglected, (ii) the source be located outside the inner region or (iii) the plume have diffused out of the inner region, the mixing of the scalar will differ.

The mean temperature profile downstream of a line source placed in a boundary layer was studied by Shlien & Corrsin (1976). They found that, when normalized, it approached an asymptotic form, independent of source position from the wall, and that an appropriately defined turbulent Prandtl number was approximately unity. Paranthoën *et al.* (1988) measured the mean and fluctuating temperature field downstream of a line source placed in a turbulent boundary layer and in a plane jet. They deduced a rescaling scheme based on the temporal integral Lagrangian scale of the vertical velocity fluctuations (see also Dupont, El Kabiri & Paranthoën 1985.) This scheme satisfactorily collapsed the mean profiles onto a simple curve, however, the profiles of fluctuating quantities did not rescale well (see figures 12 and 13 of Paranthoën *et al.* 1988). Further measurements of scalar dispersion from a line source in a boundary layer were undertaken by El Kabiri *et al.* (1998) to assess various first- and second-order closure models. Measurements of the variance, intermittency, peak concentration values, probability density functions and spectra of the scalar have been made by Fackrell & Robins (1982) for ground level and elevated point sources in a turbulent boundary layer. They also studied the balance of terms in the variance and turbulent flux transport equations. Raupach & Legg (1983) made velocity and temperature measurements from an elevated line source in a turbulent boundary layer to test first- and second-order closure models. Additional work involving the experimental study of scalar dispersion in inhomogeneous flow fields has been performed by Legg, Raupach & Coppin (1986), Veeravalli & Warhaft (1990), Bara, Wilson & Zett (1992), Tong & Warhaft (1995), and Vincont *et al.* (2000).

Scalar transport in low-Reynolds-number channel flow has been simulated by Lyons & Hanratty (1991), Papavassiliou & Hanratty (1997) and Na & Hanratty (2000). Kontomaris & Hanratty (1994) studied the effects of molecular diffusivity on a point source located at the centreline of a turbulent channel flow. Direct numerical

	Low Re	High Re
$\langle U\rangle_{y/h=1}$ [m s^{-1}]	5.2	11.4
$u_{rms_{y/h=1}}$ [m s^{-1}]	0.21	0.45
u_* [m s^{-1}]	0.26	0.54
$\epsilon_{y/h=1}$ [m^2 s^{-3}]	0.56	4.7
$\ell_{y/h=1}$ [mm]	16	20
$\lambda_{y/h=1}$ [mm]	4.2	3.3
$\eta_{y/h=1}$ [mm]	0.28	0.16
$Re(=\langle U\rangle_{y/h=1}h/\nu)$	10 400	22 800
$Re_\tau(=u_*h/\nu)$	520	1080
$Re_{\lambda(y/h=1)}(=u_{rms(y/h=1)}\lambda_{y/h=1}/\nu)$	58	100
$y_s/h=0.067$	$y_s^+=35$	$y_s^+=72$
$y_s/h=0.17$	$y_s^+=87$	$y_s^+=180$
$y_s/h=1.0$	$y_s^+=520$	$y_s^+=1080$

TABLE 1. Flow parameters. The upper half of the table gives properties of the flow for the two Reynolds numbers under consideration. The lower half gives the source locations in terms of wall units for the two Reynolds numbers. $h=0.030$ m. $\nu=15\times10^{-6}$ m^2 s^{-1}.

simulations of scalar mixing released from a point source in fully developed pipe flow have been performed by Brethouwer *et al.* (1999). Vrieling & Nieuwstadt (2003) performed direct numerical simulations of single and double line sources in fully developed turbulent channel flow. Other numerical simulations of dispersion in inhomogeneous turbulent flows have been performed by Bernard & Rovelstad (1994), Wang & Komori (1999) and Iliopoulos & Hanratty (1999).

It should be noted that the mean concentration of scalar dispersion in a long pipe can be accurately predicted using Taylor shear flow dispersion theory (Taylor 1953, 1954). This method can be extended to other turbulent shear flows, however, it is valid only for very large diffusion times (i.e. times much greater than the Lagrangian integral time scale, τ_L). Since the present work concentrates on the early stages of diffusion (i.e. the turbulent convective stage), this method is not applicable to the results presented herein. Lastly, we remark that the effects of inhomogeneity on scalar mixing, including variations in the turbulence intensity across a plume, have been studied theoretically in Hunt (1985).

The objective of the present work is to study scalar dispersion in an inhomogeneous turbulent flow. The flow under consideration is one of the simplest inhomogeneous turbulent flows: fully developed high-aspect-ratio turbulent channel flow. In such a flow, the inhomogeneity is isolated to one direction (the wall-normal direction). Consequently, the effect of the inhomogeneity on the scalar dispersion can be most readily discerned. Statistics of the scalar field are studied for two Reynolds numbers and three source locations – one at the channel centreline and two near-wall positions (see table 1).

The remainder of the paper is organized as follows. The apparatus is described in § 2. In § 3, the experimental conditions and sources of error are discussed. Results are presented in § 4, where the (i) mean temperature field, (ii) fluctuating temperature field, (iii) temperature probability density functions and (iv) velocity–temperature correlations are detailed. Lastly, the conclusions and a discussion of the results are given in § 5. As the results are presented, they will be compared to those of scalar dispersion in homogeneous, isotropic, grid-generated turbulence and homogeneous turbulent shear flow, where significant progress has been made, both theoretically and

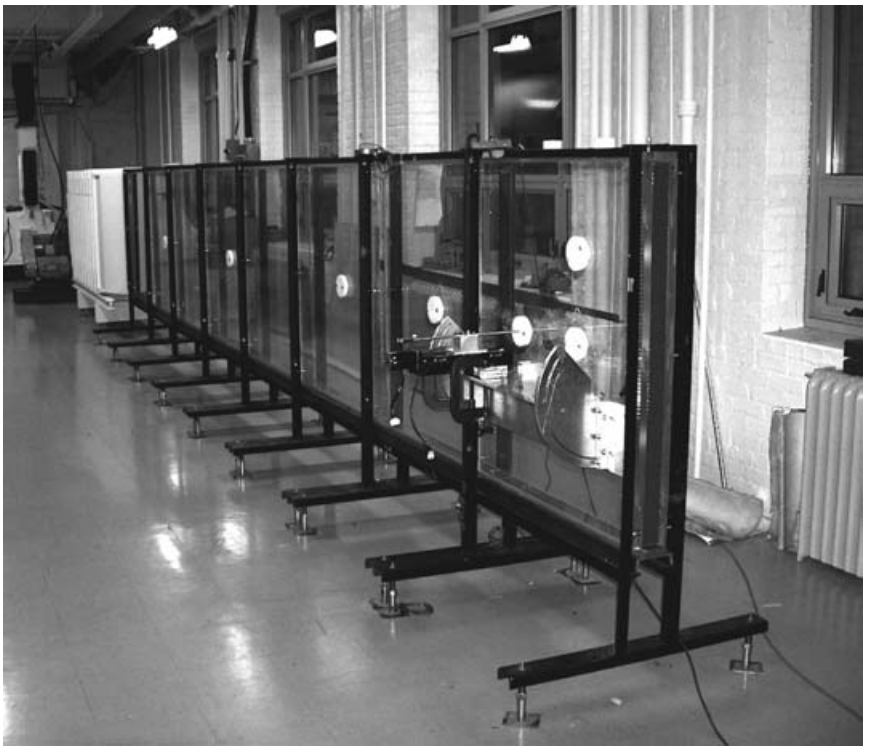

FIGURE 1. The channel in which the experiments were conducted.

experimentally. In addition, comparisons with other work in inhomogeneous flows will also be made.

2. Apparatus

The open-circuit high-aspect-ratio channel shown in figure 1 was designed for the present experiments. The channel cross-section is 1.1 m ($=L$) high by 0.06 m ($=2h$) wide. These dimensions provide an aspect ratio of 18, ensuring that – away from the top and bottom walls – the flow field will be two-dimensional.

The air flow is supplied by a centrifugal blower (Hudson Buffalo ACL size 330 BI Class 2), capable of operating over the range of required flow rates. The blower is powered by a 7.5 h.p. electric motor, and is mounted on high-density rubber footpads to damp vibrations. Precise control of the motor r.p.m. (and hence flow rate) is accomplished by an ABB ACS 600 controller. A filter box was installed at the blower intake and prevents particles greater than 3 μm in diameter from entering the test-section and potentially interfering with the instrumentation.

A perforated plate located at the blower exit serves as a preliminary flow-conditioning measure. In order to minimize the transmission of blower vibrations to the flow conditioner, a flexible rubber coupling joins the blower output to the entrance of the flow conditioner. The latter consists of a wide-angle diffuser, a settling chamber and a contraction. The purpose of the wide-angle diffuser is to reduce the speed of the flow before it enters the settling chamber. This allows the flow to remain there for a longer period of time, and also reduces the local Reynolds number of the flow through the screens and honeycomb. The area ratio of the diffuser is 3.55 – a design constraint established by the (fixed) dimensions of the blower exit area, contraction

ratio and cross-section of the channel. To minimize the diffuser length, a wall-angle of 45° was chosen. Inside a traditional diffuser, such a large wall-angle would normally result in a strong adverse pressure gradient, with a subsequent separation of the flow. The latter is inhibited by the use of four appropriately located screens inside the diffuser, which balance the pressure rise (due to the decrease in velocity) with the pressure drop (resulting from the screens). The design of wide-angle diffusers is discussed in detail in Mehta (1977). The settling chamber eliminates any transverse velocity fluctuations and swirl. Its cross-sectional area is constant and it begins with an aluminium honeycomb section. Following the latter are six screens, appropriately located to maximize the efficiency of the settling chamber (Reshotko, Saric & Nagib 1997). The honeycomb section is 76 mm long and the opposing hexagonal cell walls are 6.35 mm apart, providing the desired length to diameter ratio and cell density (Mehta 1977; Mehta & Bradshaw 1979). The mesh size of the screens is chosen to be 1 mm, based on the necessary honeycomb cell diameter to screen mesh size ratio (Mehta 1977; Reshotko *et al.* 1997). The flow conditioner height is the same as the channel (as intended), and therefore the contraction is two-dimensional. A contraction ratio of eight is chosen, based on recommended design criteria (Mehta 1977; Reshotko *et al.* 1997). To satisfy all contraction profile constraints, its shape is based on a fifth-order polynomial. After exiting the contraction, the flow enters the channel as a uniform, low-turbulence-intensity (0.25 %) velocity field.

The channel dimensions are 8 m × 1.1 m × 0.06 m. The sidewalls of the channel each consist of 8 mated one-inch thick Plexiglas sheets of dimensions 1.1 m × 1 m. The top and bottom walls each consist of four Plexiglas caps of dimensions 0.06 m × 2 m. To ensure that the joints of the sidewall sheets do not interfere with the flow field, 'biscuits' and adjustable tightening screws are used along the joints in the spanwise direction to keep the height between mating ridges less than 5 viscous lengths. This height is dependent upon the flow Reynolds number. The maximum measured height is within the limits of which the channel walls can be considered hydrodynamically smooth (Tennekes & Lumley 1972). To establish fully developed flow as soon as possible, boundary-layer tripping rods are placed near the entrance of the channel (Shah, Chambers & Antonia 1983). Along each wall in the spanwise direction, a 3.2 mm diameter rod is located 3 mm from the wall. These rods are located 60 mm downstream of the entrance, to allow for some boundary-layer growth before tripping it. The test section extends from 7.00 to 8.00 m downstream of the channel entrance. Custom-made machined ports are located at 7.33 m and 7.67 m from the channel entrance along the spanwise centreline, where all the measurements in this work are taken.

Injection of the scalar is accomplished by means of fine Nichrome wire line sources, aligned in the spanwise direction and passing through small holes in the top and bottom walls of the channel. For measurements close to the source ($x/h \leqslant 10.8$), the source diameter was 0.127 mm. Farther downstream, a greater power input is required to improve the signal-to-noise ratio. Therefore, a source diameter of 0.254 mm is employed for these locations. The source is heated via a d.c. power supply, which provides 45 W m^{-1} and 100 W m^{-1} for the small and large diameter sources, respectively. Consequently, when temperature statistics are compared in a non-normalized fashion (i.e. figures 6 and 9), the results for $x/h > 10.8$ must be divided by a factor of 2.22 (=100/45) to be consistent. We also remark that the line sources expand when heated. Therefore, to maintain taut straight sources, a small weight is hung from the bottom of the source, outside the channel.

Hot-wire anemometry was used to measure the longitudinal and transverse velocities. 3.05 μm diameter tungsten hot wires were operated at an overheat of 1.8 using a

TSI IFA 300 constant temperature hot-wire anemometer. A TSI 1218 boundary-layer probe was used to establish the flow conditions (figures 3 and 4) and a TSI 1241 X-wire probe was employed in the measurements of turbulent fluxes (figures 18–20). The spatial resolution of the hot wires (in terms of viscous lengths, $l^+ \equiv lu_\star/\nu$, where l is the wire length) was 9 and 18 for the low and high Reynolds numbers, respectively. Khoo, Chew & Teo (2000) recommend (viscous) wire lengths no larger than 20–25 for accurate turbulence measurements. In terms of Kolmogorov variables, $l/\eta(y=h)$ was 1.8 and 3.1 for the low and high Reynolds numbers, respectively†. (Next to the wall, these values became 3.3 and 5.6.) For the large-scale velocity measurements presented in figures 18–20 (which were made outside the near-wall region), this resolution is adequate. The length-to-diameter ratio of the hot-wires was approximately 200 and the two wires composing the X-wire were separated by 1 mm. The effective-angle method of Browne, Antonia & Chua (1989) was used to calibrate the X-wires. The method of Lienhard (1988) was used to compensate the velocity measurements for the variable temperature of the flow by a modified King's Law with temperature-dependent coefficients.

Cold-wire thermometry was used to measure the temperature field. The cold wires were made of Wollaston wire (with 0.63 μm diameter platinum cores) and soldered to TSI 1210 single-wire probes. The former were operated by a cold-wire thermometer built at the Université Laval (Québec, Canada) and based on a constant-current anemometry circuit given by Lemay & Jean (2001) and Lemay & Benaïssa (2001). A single cold wire was used in the measurements of the mean temperature excess ($\Delta T = \langle T \rangle - T_\infty$), whereas all measurements of the fluctuating temperature employed a cold-wire probe positioned 1 mm away from a X-wire. (Consequently, the fluctuating temperature measurements begin farther from the channel wall to avoid interference effects between the wall and the probe assembly.) The cold-wire probe current was 150 μA and the length-to-diameter ratio of the etched portion of its wires was approximately 800 (i.e. $l_{wire} \approx 0.5$ mm). This choice was a compromise between the competing effects of (i) spatial resolution and (ii) conduction between the cold-wire and its prongs (Browne & Antonia 1987). A complete discussion of this is given in Mydlarski & Warhaft (1998). Wyngaard's corrections for spatial resolution error (Wyngaard, 1968, 1971) were applied to the spectra. Lemay & Jean (2001) showed that a 0.63 μm Pt–10%Rh cold wire is able to resolve frequencies up to 7.3 kHz and 8.7 kHz for flows of 5 m s^{-1} and 10 m s^{-1}, respectively.

With the exception of the measurement of the mean quantities, the hot-wire anemometer and cold-wire thermometer outputs were both high- and low-pass filtered (using Kron-Hite 3382 and 3384 band-pass filters). A National Instruments PC-MIO-16E4 data acquisition board controlled using LabVIEW was used to digitize their analogue outputs. Moments of fluctuating quantities were recorded using data sets consisting of 4.096×10^4 samples recorded at 200 Hz (for a corresponding record duration of 3.4 min). The sampling frequency corresponds to roughly the inverse of the integral time scale of the measured quantities. Spectral data sets (used to compute spectra as well as any quantities involving time derivatives, e.g. dissipations) consisted of 4.096×10^5 data points sampled at twice the low-pass filtering frequency (which was set to a frequency slightly larger than the Kolmogorov frequency, $f_\eta = \langle U \rangle/(2\pi\eta)$).

† $\eta(y) \equiv (\nu^3/\epsilon(y))^{1/4}$, where $\epsilon(y)$ is the dissipation rate of turbulent kinetic energy. The latter is estimated, assuming local isotropy, by $\epsilon = 15\nu \int_0^\infty \kappa_1^2 E_u(\kappa_1)\,\mathrm{d}\kappa_1$, where κ_1 is the longitudinal wavenumber and $E_u(\kappa_1)$ is the power spectrum of the longitudinal velocity fluctuations.

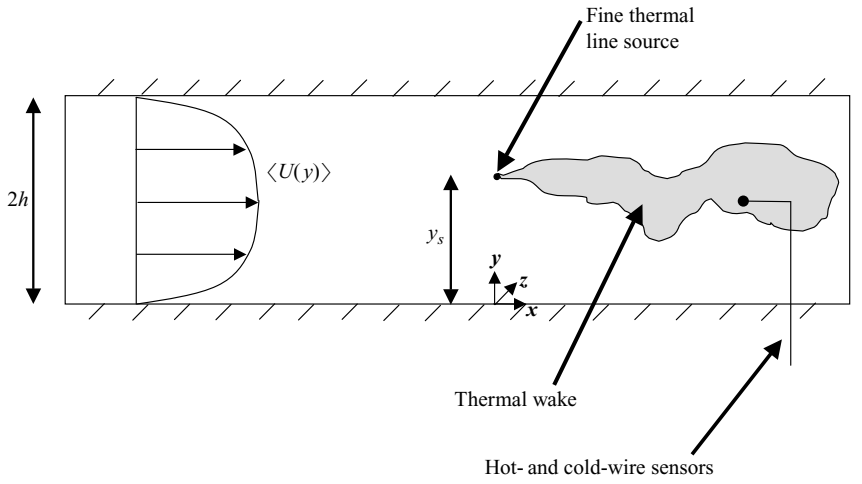

FIGURE 2. A schematic of the experiment in which the coordinate system used herein is defined.

Probability density functions (PDFs) were estimated using 4.096×10^5 samples recorded at 200 Hz. Convergence of these quantities was verified in Lavertu (2002).

For the measurements of mean temperature excesses, the mean output voltage of the cold-wire thermometer was determined by averaging the non-high-pass-filtered output voltages. The ambient 'cold' fluid temperature, T_∞, was also recorded to compensate for drifts in room temperature. The cold temperature was measured by a mini-bead thermistor (Sensor Scientific), located in the channel, upstream of the source.

Lastly, the thermal plume and flow field were scanned in the transverse direction using a linear traversing mechanism driven by a precision stepper motor and linear traversing mechanism (0.01 mm per step – Velmex BiSlide). Note that measurements could not be made in the 10 mm region closest to the farthest wall because of interference from the probe. Therefore, no measurements for $1.67 \leqslant y/h \leqslant 2$ are shown.

A schematic of the coordinate system used in the present work is shown in figure 2.

3. Experimental conditions and sources of error

The first objective of the present section is to characterize the flow field. This was thoroughly done in Lavertu (2002) and the results are summarized herein. The second objective of this section is to discuss and quantify (where possible) the potential sources of error in the present work.

The (statistically) two-dimensional nature of the flow in the present apparatus was verified by McLeod (2000). He found that profiles of the mean and r.m.s. longitudinal velocity, as well as its skewness ($\langle u^3\rangle/\langle u^2\rangle^{3/2}$) and kurtosis ($\langle u^4\rangle/\langle u^2\rangle^2$) all collapsed for measurements made at $z/L = -0.25$, 0, $+0.25$.

The static pressure distribution in the channel was subsequently measured and shown to be linearly decreasing by the end of the channel, where the experiments are performed. However, this is the most rudimentary test for fully developed flow (Shah *et al.* 1983). The mean and r.m.s. velocity profiles in the channel for a Reynolds number of 22 800 are shown in figure 3 at two downstream measurement locations ($x = 7.33$ m and $x = 7.67$ m, which correspond to $x/h = 244$ and 256, respectively. (Recall that h is the channel half-width: 0.03 m.) The maximum difference in the measured profiles is 0.9% for the mean and 3.7% for the r.m.s. The differences in the skewness and

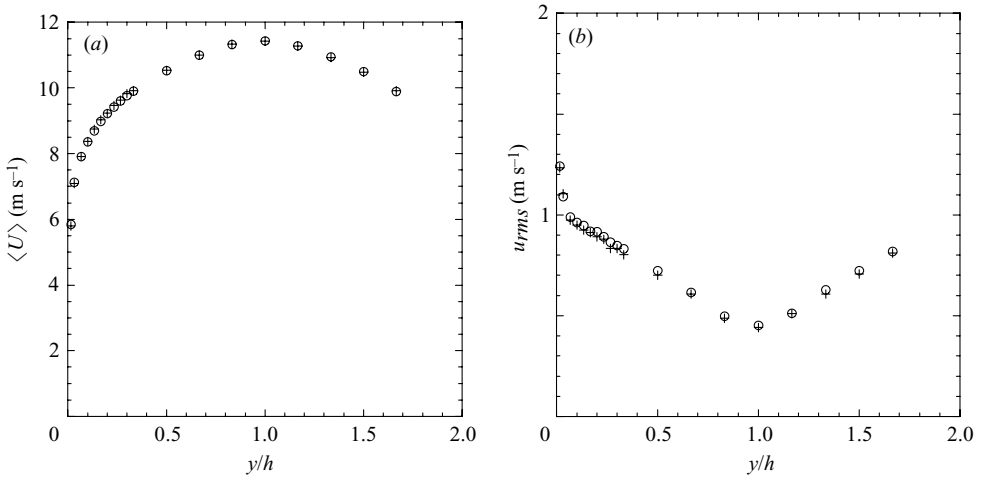

FIGURE 3. Velocity profiles across the channel at two downstream locations. (*a*) Mean velocity profile. (*b*) Root mean square velocity profile. ○, $x/h = 244$; +, $x/h = 256$. $Re = 22\,800$.

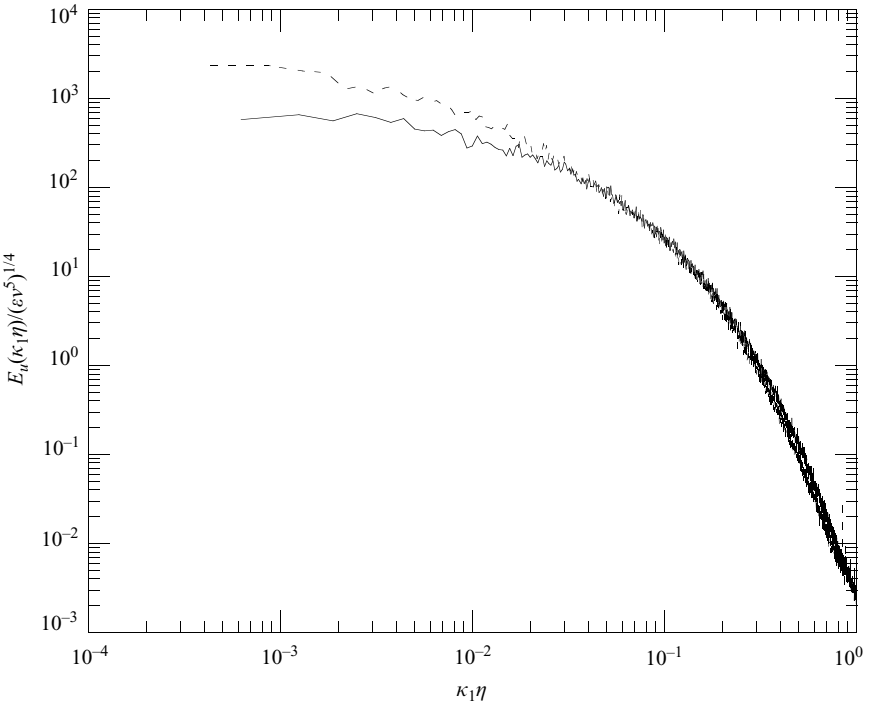

FIGURE 4. Power spectra of the longitudinal velocity fluctuations at the channel centreline ($y/h = 1.0$). Solid line: $Re = 10\,400$. Dashed line: $Re = 22\,800$.

kurtosis of the longitudinal velocity fluctuations measured at the centreline for these two downstream locations was less than 0.01 (i.e. constant to within the experimental uncertainty). Comparable results were obtained at a Reynolds number of 10 400 and can be found in Lavertu (2002).

Given that fully developed flow has been achieved in the test section, we present spectra of the velocity field in figure 4. The power-spectra of the longitudinal

velocity fluctuations for the two Reynolds numbers collapse well at small scales (when normalized by Kolmogorov variables).

Having characterized the flow, we must also ensure that the presence of the source and the thermal field it generates do not affect the velocity field. As mentioned in the previous section, two different line source diameters were used: 0.127 mm and 0.254 mm. The source Reynolds number, $Re_{source} \equiv \langle U(y) \rangle d/\nu$, is based on the local mean velocity and the kinematic viscosity of the air at the film temperature, $T_{film} \equiv (T_{source} + T_\infty)/2$. ($T_{source}$ was determined from an energy balance over the source in conjunction with the applied power and the average convective heat transfer coefficient over the source, calculated by means of the Zhukauskas (1972) correlation.) For the different flows, source diameters and source locations, Re_{source} varied from 17 to 111. Since some values of Re_{source} are above 40, vortex shedding from the source may occur (Blevins 1990). However, no mechanical effects of the source were observed in any of the experiments. None of the measured velocity spectra exhibited any spikes indicative of vortex shedding. We therefore conclude that if vortex shedding is present, its effects are so small that they are masked by the turbulence.

To confirm that the source diameter is not affecting the results, we examined temperature statistics for different source diameters. Lavertu (2002) compared r.m.s. and skewness profiles of the thermal fluctuations generated by sources with diameters $d = 0.127$ mm and $d = 0.254$ mm. (These diameters correspond to $d_{source}/\eta_{y=y_s} = 0.85$ and 1.7, respectively at $Re = 10\,400$, where $\eta_{y=y_s}$ is the Kolmogorov length scale at the wall-normal source location.) Lavertu (2002) found the differences to be negligible. Therefore, we are assured that our results are independent of the source diameter for the downstream locations under consideration.

Given that the temperature field is statistically homogeneous in the direction of the gravitational acceleration vector (z), it is difficult to determine the effect of buoyancy. As a 'worst-case' estimate, the ratio of the buoyant production of turbulent kinetic energy to its dissipation, $g\langle v\theta \rangle/(T\epsilon)$, was calculated assuming that the direction of the acceleration due to gravity is in the transverse (y) direction. A typical value was 1.7% (for $y_s/h = 0.067$, $x/h = 4.0$, $Re = 22\,800$), showing the role of buoyancy to be small. The scalar fluctuations can therefore be considered passive. Since the mean temperature excesses in this experiment are under 1 K, this should come as no surprise.

The interaction of the channel walls with the thermal plume is studied by making an approximate energy balance through the channel wall. Lavertu (2002) showed that the heat transfer through the walls is a small fraction of the total heat transfer to the flow. Assuming the temperature of the inner channel surface to be equal to the centreline mean temperature in the plume (an overestimate), he found the heat transfer through the wall to be 5% of the total power input to the thermal line source. In addition, the ratio of the resistance to heat transfer by conduction through the channel wall ($t_{Plexiglas}/(k_{Plexiglas}A)$) to the resistance to convective heat transfer over its (inner) surface ($1/(\overline{h}_{convective}A)$) is approximately 25 for the low-Reynolds-number case and 42 for the high-Reynolds-number case†. Both values are sufficiently larger than 1 that the channel walls may be regarded as adiabatic.

We proceed to discuss the error of the experimental results to be presented herein. First, the measurements of the mean temperature excess experience the largest uncertainty. Their peak mean temperature rise is of the order of 0.5 K while the typical error in their measurement is ± 0.05 K. The latter, which is quantified by the error

† This ratio – $\overline{h}_{convective} t_{Plexiglas}/k_{Plexiglas}$, where $\overline{h}$ is the average convective heat transfer coefficient, k is the thermal conductivity and t is the thickness – can be interpreted as a modified Biot number.

bars in figure 6, results from inaccuracies in estimating the free-stream temperature. Consequently, the measurement of mean temperature excess profiles is difficult given that the signal-to-noise ratio is often below 10. More emphasis is therefore placed on the qualitative behaviour of the mean temperature profiles. Also note that the mean temperature excess statistics are not shown for $x/h = 10.8$ (for $y_s/h = 1.0$) and $x/h = 22.0$ (for all y_s/h). Both downstream locations correspond to the furthest downstream measurements for the 0.127 mm and 0.254 mm diameter sources, respectively. At such locations, the error can be too large to provide accurate results.

At this point, it is important to note that the fluctuating temperature field is not subject to the effects of room temperature variations (and is therefore significantly more precise). For its measurement, the cold-wire thermometer signal is high-pass filtered (at 0.1 Hz), which eliminates any error from drifts in the room temperature. Such room temperature variations occur at frequencies lower than the high-pass filter frequency.

The errors in mean profile widths, peak r.m.s. temperature, r.m.s. profile widths and r.m.s. peak locations are quantified by the error bars in figures 7, 9, 10 and 11. They were estimated from multiple measurements of the respective quantities. The average error in the velocity–scalar correlations has been estimated at $\pm 5\%$ (of the value of the correlation), with a maximum absolute error of ± 0.05 in their peak. The measured correlations between θ and v were generally less accurate than those between θ and u.

Lastly, errors in positioning the probe are small. Downstream distances are accurate to within 1 mm (or $x/h = 0.033$). Wall-normal distances have an absolute error of approximately 0.5 mm ($y/h = 0.017$) owing to uncertainties in the initial positioning of the probe. However, the error in relative displacements is negligible owing to the high precision (0.01 mm per step) of the stepper-motor-controlled traversing mechanism.

4. Results

The results are divided into a discussion of the mean temperature field (§ 4.1), the fluctuating temperature field (§ 4.2), temperature probability density functions (PDFs) (§ 4.3) and velocity–temperature correlations (§ 4.4). Experiments were performed at two different Reynolds numbers, with the source located at three positions from the wall. Table 1 summarizes the flow properties for the six experimental conditions studied herein.

4.1. *Mean temperature field*

In isotropic grid-generated turbulence (Warhaft 1984), the transverse mean temperature profiles are Gaussian. The mean temperature profiles behind a concentrated source in homogeneous turbulent shear flow are also initially Gaussian. Farther downstream, however, the profiles become asymmetric, and their peaks shift to the region of lower velocity (Karnik & Tavoularis 1989). Mean temperature profiles (normalized by the peak mean temperature) are shown in figure 5 for the $y_s/h = 0.067$, 0.17 and 1.0 source locations. Over the downstream distances considered, they are approximated well† by truncated Gaussian profiles with peaks that remain relatively fixed behind the source. Any potential displacement of the peaks of the profiles is not discernable

† Because the wall can be approximated as adiabatic, a more accurate profile should, in principle, be given by a Gaussian profile with reflection from an imaginary source located at $-y_s/h$ – see, for example, Fackrell & Robins (1982). However, for the purposes of the present work (where the emphasis is placed on the fluctuations and their related fluxes) the increased complexity is of little benefit, especially with respect to the growth rates of the plume width – see figure 7.

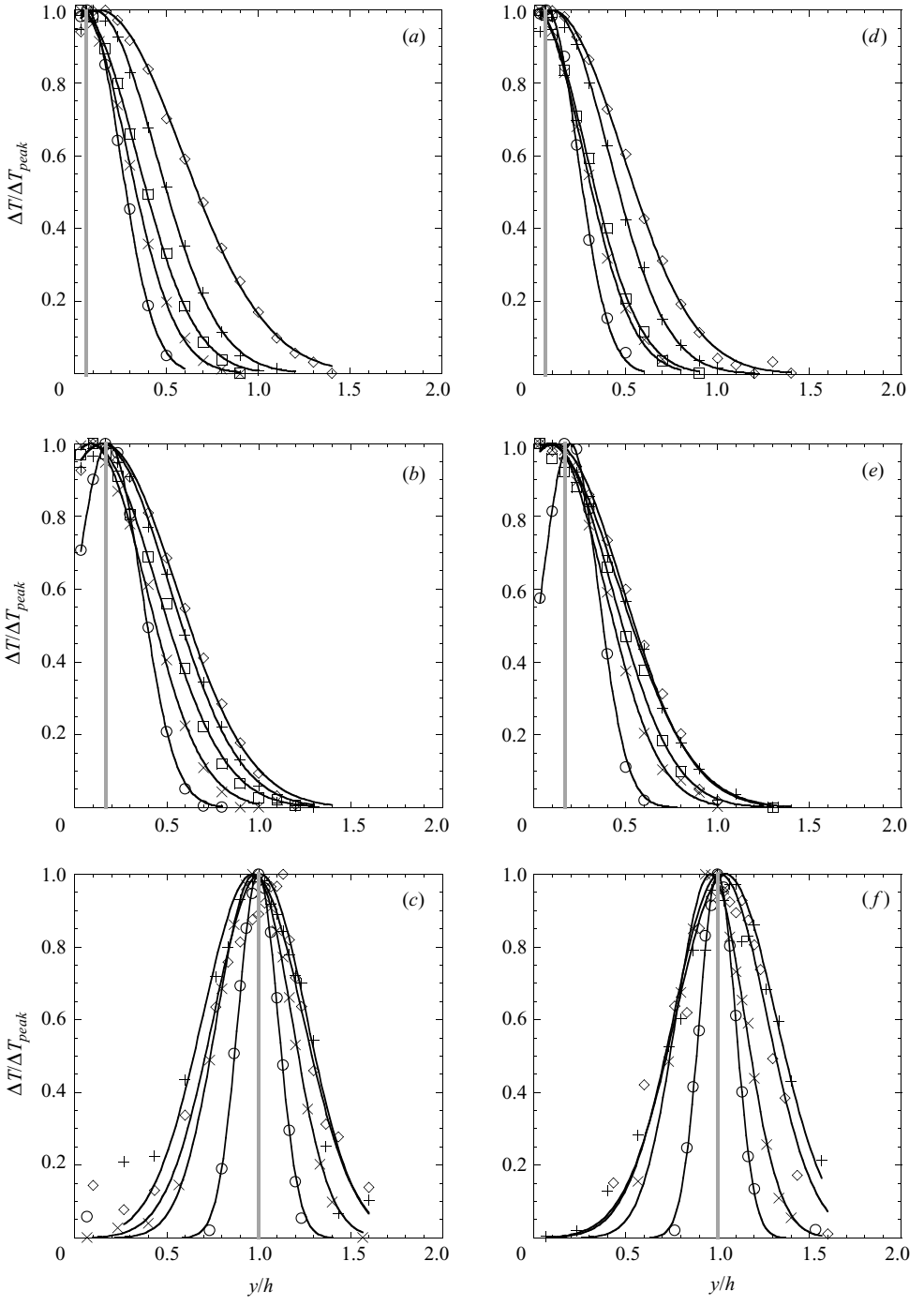

FIGURE 5. Non-dimensionalized mean temperature excess profiles at different downstream locations for the three source locations and the two Reynolds numbers. The vertical grey lines indicate the transverse location of the source. (*a*)–(*c*) correspond to $Re = 10\,400$. (*d*)–(*f*) correspond to $Re = 22\,800$. (*a*), (*d*) $y_s/h = 0.067$. (*b*), (*e*) $y_s/h = 0.17$. (*c*), (*f*): $y_s/h = 1.0$. ○, $x/h = 4.0$; ×, $x/h = 7.4$; □, $x/h = 10.8$; +, $x/h = 15.2$; ◇, $x/h = 18.6$. The solid lines corresponds to the best fit Gaussian profile.

owing to the combination of (i) the smaller range of downstream positions considered herein as compared to the unbounded flows of Fackrell & Robins (1982), Raupach & Legg (1983), Karnik & Tavoularis (1989) and El Kabiri *et al.* (1998), (ii) the lack of near-wall data because of the interference of the probes with the wall, and (iii) the experimental scatter. (Karnik & Tavoularis (1989) only observed the drift of the peak of the mean temperature profiles for $x/M \geqslant 48$.) The effect of the source location on the mean temperature profile is as expected – source locations farther from the wall have their peaks at locations farther from the wall. Also, as we might anticipate, the profiles at the higher Reynolds number are less wide than those at the lower Reynolds number. This observation derives from the fact that the plumes have had less time to spread because the mean velocity is higher at the larger Reynolds number.

The peak mean temperature excess (ΔT_{peak}) is plotted in figure 6 as a function of distance downstream of the source (x/h) for different source locations and Reynolds numbers. In isotropic grid-generated turbulence, as well as in homogeneous turbulent shear flow, the decay rate of the peak mean temperature is reasonably well described by a power law of the form $\Delta T_{peak} \propto x^n$. In the present flow, this is clearly not the case. Nevertheless, fitting a power law to the data (for the sole purpose of comparison with data from homogeneous flows) results in a decay exponent of $n \sim -0.7$, -0.5 and -0.6 for the $y_s/h = 0.067$, 0.17 and 1.0 source locations, respectively. (The values of n showed no significant Reynolds-number dependence.) Such values are less than the values obtained in homogeneous flows for which $n \approx -0.75$ to -1.0 for $x/M \gtrsim 1$. (See Karnik & Tavoularis (1989), figure 8, which summarizes their results in addition to the grid turbulence results of Warhaft (1984) and Stapountzis *et al.* (1986).) Presumably, for homogeneous flows at large enough values of x/M (so that the plume is well into the turbulent diffusive stage), n should decrease to a value of the order of -0.5. (Such measurements, however, have not been made in homogeneous flows – see Warhaft 1984.) In turbulent boundary layers, Dupont *et al.* (1985) showed that data from different experiments collapsed (using a Lagrangian rescaling) and exhibited a decay of the peak mean temperature with a power-law slope, n, of -1 that evolved to a decay with $n \approx -0.5$ farther downstream. In the present flow, a turbulent diffusive regime is unexpected owing to its bounded nature. This will be discussed shortly with respect to the r.m.s. temperature profiles. In numerical simulations of fully developed turbulent channel flow, Vrieling & Nieuwstadt (2003) observed $n \approx -1$ for a source located at the channel centreline. However, we note that their data does not extend beyond $x/h \approx 8$ and is for a Reynolds number of $Re_\tau = 180$. For a centreline point source release in fully developed pipe flow ($Re_D (\equiv \langle U \rangle D/\nu) = 5300$), Brethouwer *et al.* (1999) also observed a mean peak temperature decay with a slope of approximately -1.

The width of the mean profiles is quantified in figure 7, which plots the standard deviations† of the best-fit Gaussian curves to the mean temperature profiles (σ_{mean}) as a function of x/h for the different source locations and Reynolds numbers. Like the previous figure, these do not exhibit a power-law dependence, as is the case in homogeneous flows. Here, we note that the increase in σ_{mean} is retarded for larger values of x/h – an observation presumably attributable to the channel walls 'impeding' the dispersion of the energy. As mentioned with respect to figure 5, the mean profile widths for the higher Reynolds number are generally smaller than the corresponding widths at the lower Reynolds number.

† The half-width of a profile is an alternative measure of a profile's width and is defined to be half the width of the profile when it is 50% of its maximum value. For a Gaussian profile, it can be shown that the half-width is equal to 1.177 times the standard deviation.

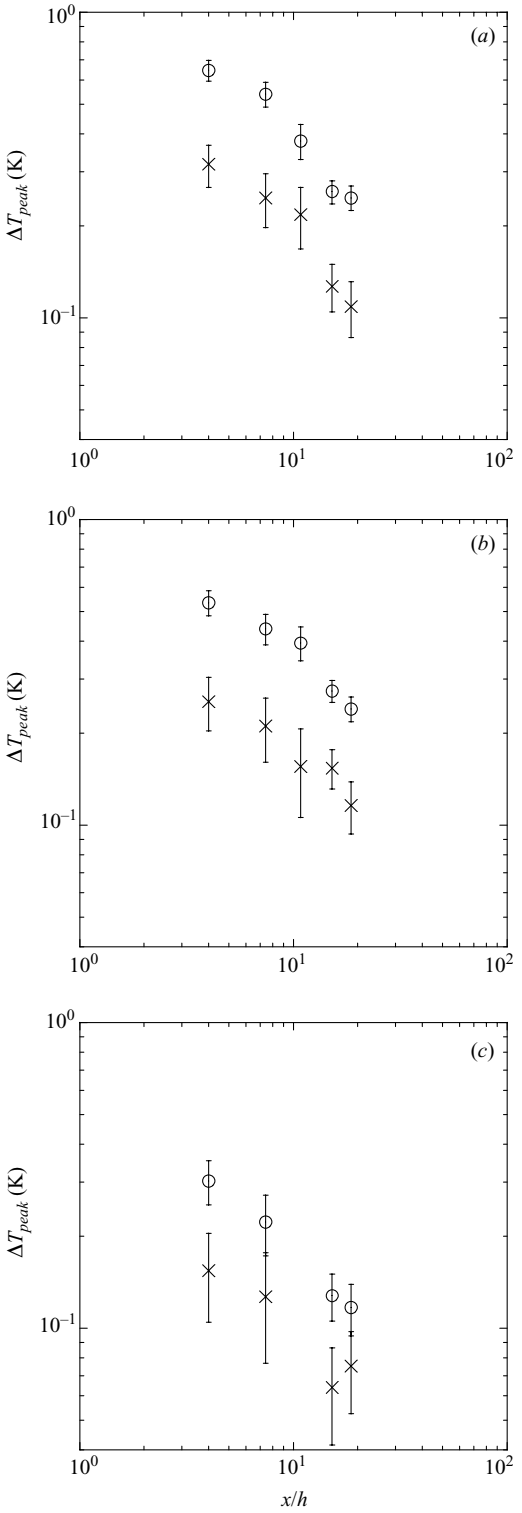

FIGURE 6. The downstream evolution of the peak mean temperature excess for both Reynolds numbers. (*a*) $y_s/h = 0.067$. (*b*) $y_s/h = 0.17$. (*c*) $y_s/h = 1.0$. ○, $Re = 10\,400$; ×, $Re = 22\,800$.

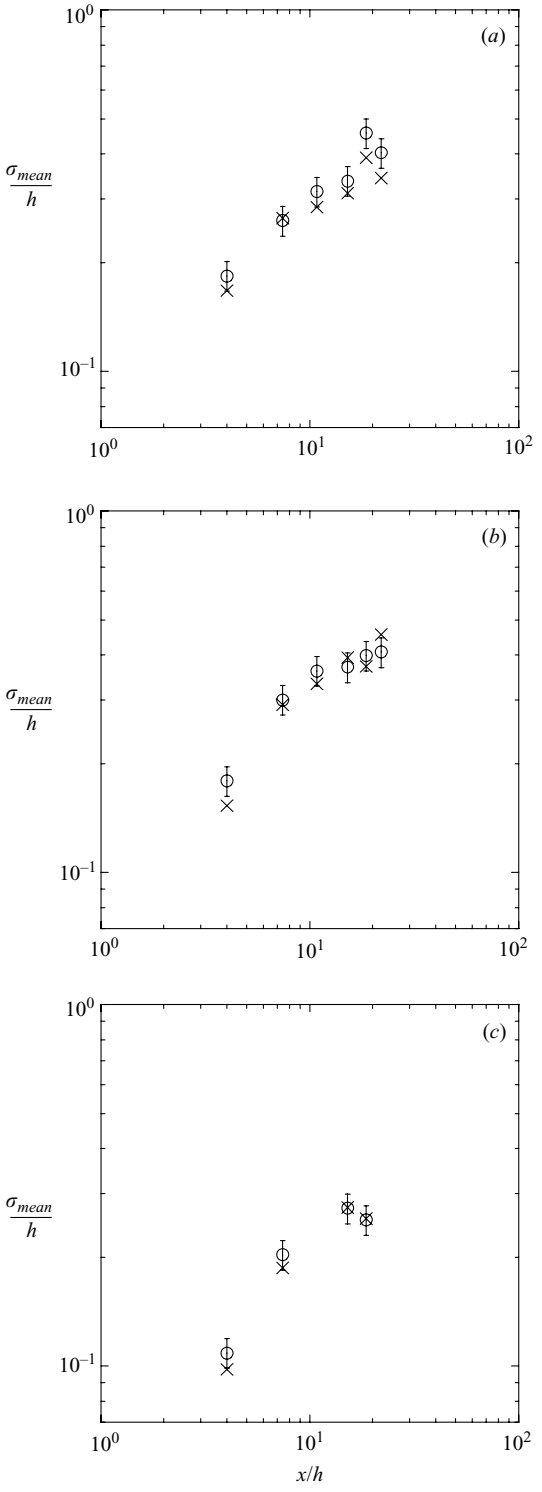

FIGURE 7. The downstream evolution of the width of the mean temperature profiles for both Reynolds numbers. (*a*) $y_s/h = 0.067$. (*b*) $y_s/h = 0.17$. (*c*) $y_s/h = 1.0$. ○, $Re = 10\,400$; ×, $Re = 22\,800$. In the interest of clarity, error bars are shown only for the low-Reynolds-number data since the accuracy of the measurements is similar for both Reynolds numbers.

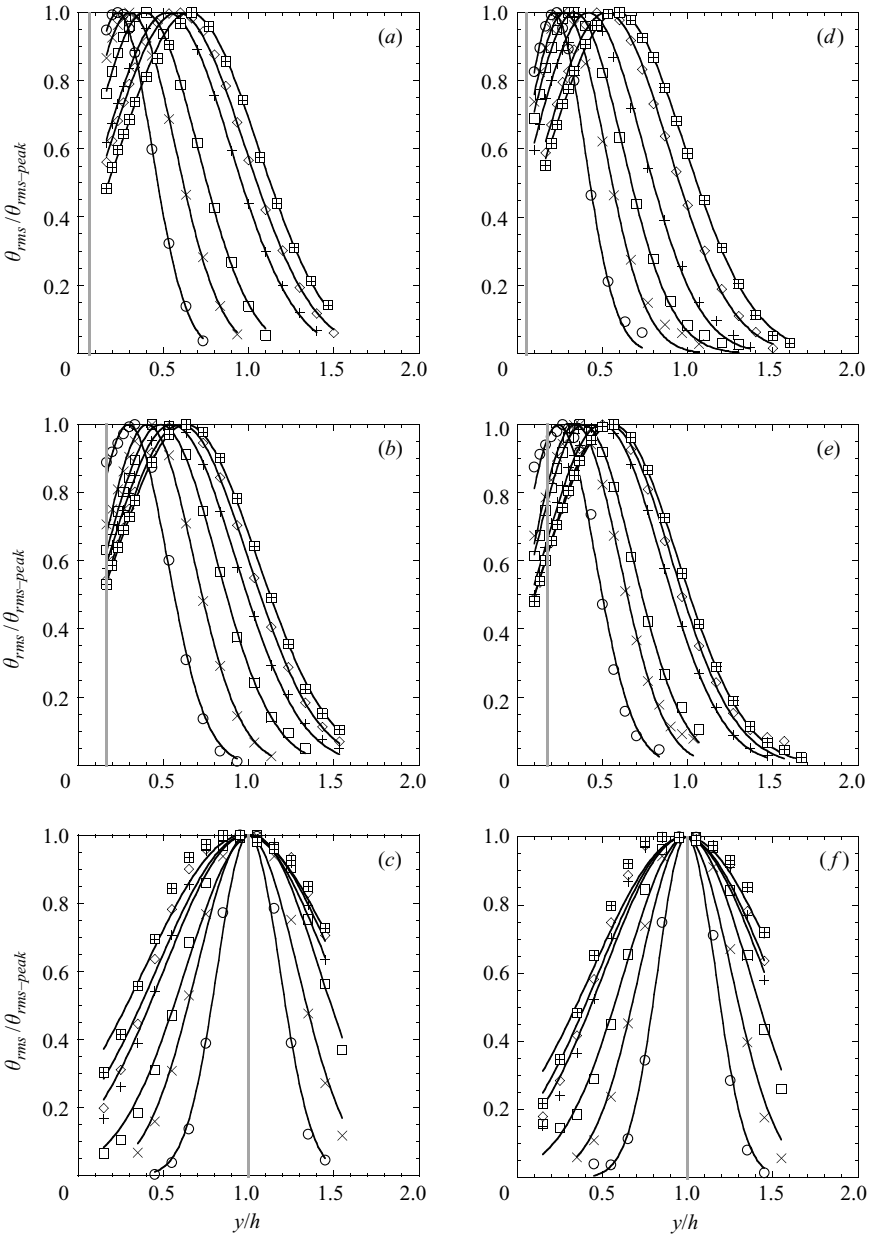

FIGURE 8. Non-dimensionalized r.m.s. temperature profiles at different downstream locations for the three source locations and the two Reynolds numbers. The vertical grey lines indicate the transverse location of the source. (*a*)–(*c*) correspond to $Re = 10\,400$. (*d*)–(*f*) correspond to $Re = 22\,800$. (*a*), (*d*) $y_s/h = 0.067$. (*b*), (*e*) $y_s/h = 0.17$. (*c*), (*f*) $y_s/h = 1.0$. ○, $x/h = 4.0$; ×, $x/h = 7.4$; □, $x/h = 10.8$; +, $x/h = 15.2$; ◇, $x/h = 18.6$; ⊞, $x/h = 22.0$. The solid lines corresponds to the best fit Gaussian profile.

4.2. *Fluctuating temperature field*

The transverse profiles of the r.m.s. temperature fluctuation, θ_{rms}, normalized by their peak value, $\theta_{rms-peak}$ are shown in figure 8. Like the mean profiles, for the ranges under consideration, these are described well by truncated Gaussian curves (with

deviations beginning to appear at large x/h for the plume with $y_s/h = 1.0$). However, unlike the mean profiles, there exists a clear drift of the peak of these profiles towards the centreline (for the cases corresponding to source locations off the centreline†). A drift of the peaks of the scalar r.m.s. profiles away from the wall for concentrated source releases in turbulent boundary layers was also observed in the work of Fackrell & Robins (1982), Raupach & Legg (1983) and El Kabiri *et al.* (1998).

In homogeneous turbulence, Warhaft (1984) and Karnik & Tavoularis (1989) observed r.m.s. profiles that were initially double-peaked (up to $x/M \sim 2$), then single-peaked, then again double-peaked for distances far downstream from the source. In the present work, our first downstream measurement is made at $x/h = 4.0$, i.e. beyond the initial region in which a double-peaked r.m.s. profile might be expected. (As a first estimate, $\ell \sim M$ in the works of Warhaft (1984) and Karnik & Tavoularis (1989), whereas $\ell \sim h$ in the present work‡. Therefore, for the purposes of comparing downstream distances between the different flows, scaling by M and h should be similar.) There is no reason to suspect, however, that the r.m.s. profiles in the present experiment are not double-peaked very close to the source.

Double-peaked r.m.s. profiles are not observed for far downstream distances. The re-emergence of double-peaked r.m.s. (or equivalently variance) profiles in homogeneous flows was explained in Karnik & Tavoularis (1989). Noting that temperature fluctuations result from (i) 'local' turbulent production in regions of non-zero mean temperature gradient and (ii) turbulent transport of temperature, they remarked that the latter causes temperature fluctuations at locations corresponding to the peak mean temperature, where the mean transverse temperature gradient will be zero. (This argument neglects the weaker mean streamwise temperature gradient – a reasonable assumption.) If the size of the eddies performing the turbulent transport of temperature is small compared to the distance over which the transverse temperature gradient (here $\mathrm{d}\langle T\rangle/\mathrm{d}y$) changes, θ_{rms} should be roughly proportional to the local value of the transverse temperature gradient, $d\langle T\rangle/dy$. For quasi-Gaussian mean profiles, this will result in a double-peaked r.m.s. profile. On the other hand, should the size of the eddies performing the turbulent transport be large compared to the distance over which $\mathrm{d}\langle T\rangle/\mathrm{d}y$ changes, the r.m.s. profile will be smoother. The former case corresponds to plume widths larger than the integral scale of the turbulence, whereas the latter case corresponds to the opposite case. (A similar explanation was also given by Thomson 1990.) In the present bounded inhomogeneous flow, plume widths much larger than the integral scale are physically impossible. Therefore, in inhomogeneous flows, the re-emergence of double-peaked r.m.s. profiles is unlikely.

The downstream decay of the peak values of the θ_{rms} profiles is plotted in figure 9 for different source locations and Reynolds numbers. On a log–log plot, the curves are approximately linear. Assuming their decay is described by a power law of the form $\theta_{rms-peak} \propto x^n$ results in $n \sim -1$ for all locations and Reynolds numbers. The decay of the peak values of the temperature variance profiles in homogeneous flows was summarized in Karnik & Tavoularis (1989), figure 10. In homogeneous, isotropic grid turbulence, $n \sim -0.8$ for $x_\theta/M \geqslant 3$. In homogeneous shear flow, Karnik &

† Given the underlying symmetries of the experiment, all profiles for $y_s/h = 1.0$ must be symmetric about the channel centreline ($y/h = 1.0$).

‡ In the present inhomogeneous flow, $\ell = \ell(y)$. At the channel centreline, $\ell = 0.53h$ and $0.66h$ for $Re = 10\,400$ and $22\,800$, respectively. In Warhaft (1984), $\ell = 0.4M$ to $0.65M$, depending on the downstream position. In Karnik and Tavoularis (1989), $\ell = 0.4M$ to $2M$.

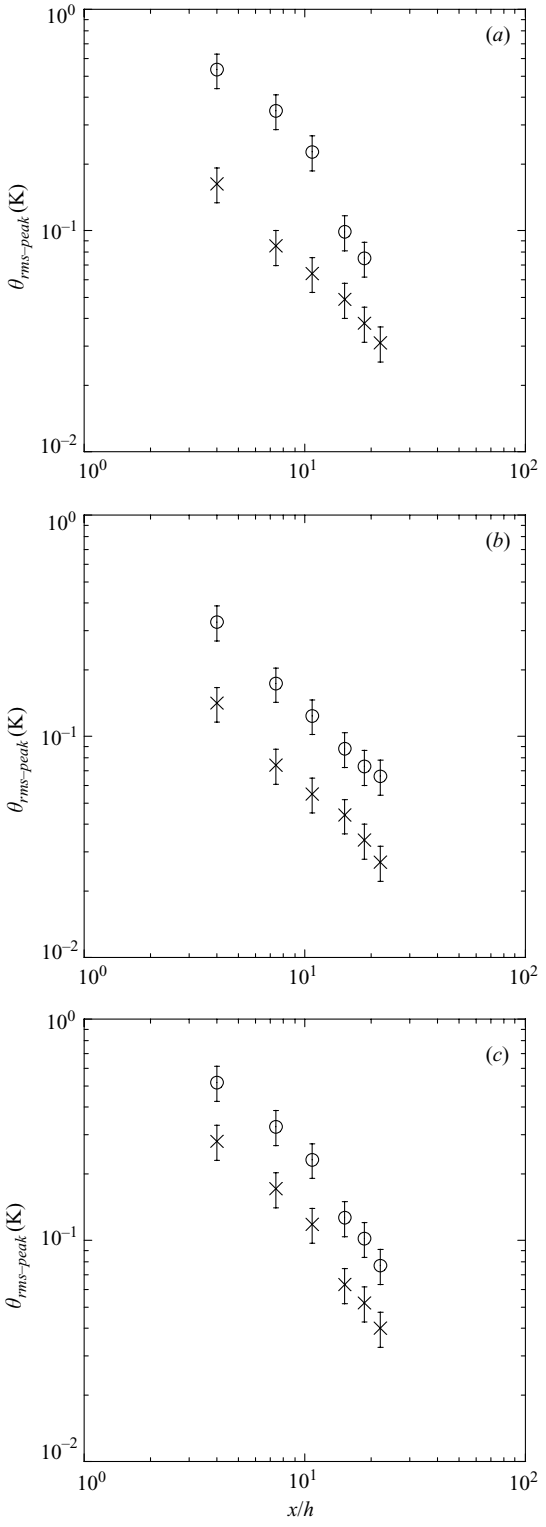

FIGURE 9. The downstream evolution of the peak r.m.s. temperatures for both Reynolds numbers. (*a*) $y_s/h = 0.067$. (*b*) $y_s/h = 0.17$. (*c*) $y_s/h = 1.0$. ○, $Re = 10\,400$; ×, $Re = 22\,800$.

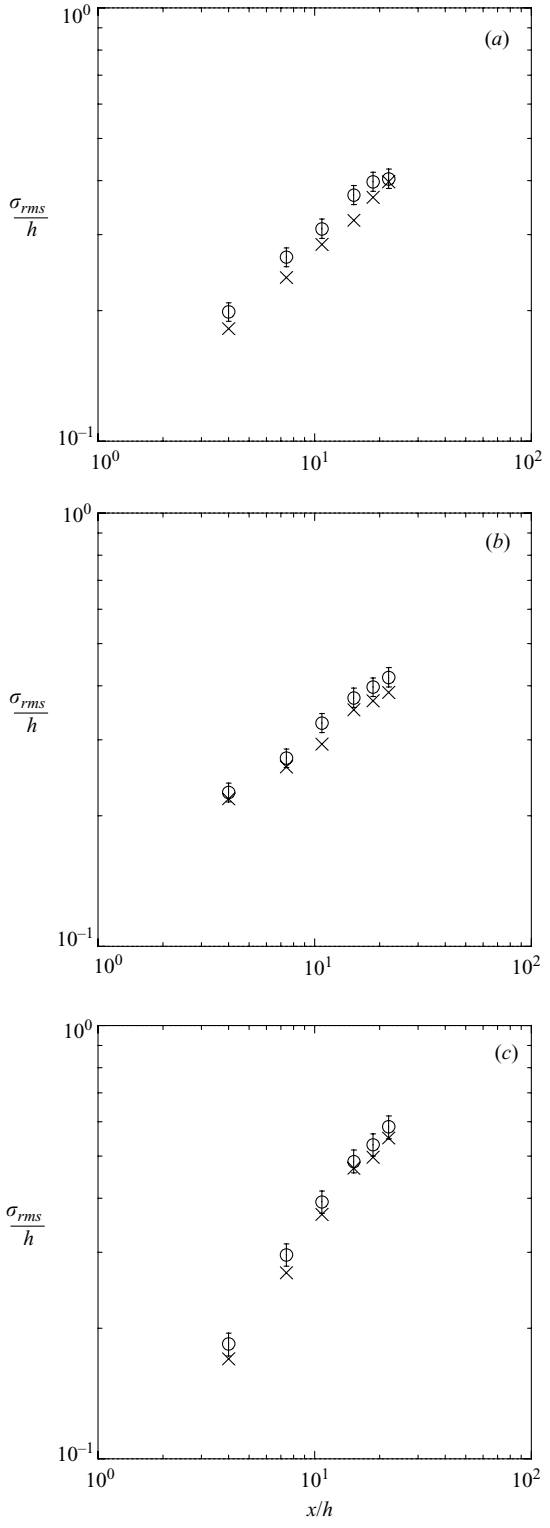

FIGURE 10. The downstream evolution of the width of the r.m.s. temperature profiles for both Reynolds numbers. (*a*) $y_s/h = 0.067$. (*b*) $y_s/h = 0.17$. (*c*) $y_s/h = 1.0$. ○, $Re = 10\,400$; ×, $Re = 22\,800$. In the interest of clarity, error bars are shown only for the low-Reynolds-number data since the accuracy of the measurements is similar for both Reynolds numbers.

y_s/h	Re	A	m
0.067	10 400	0.111	0.431
	22 800	0.096	0.454
0.17	10 400	0.134	0.372
	22 800	0.132	0.348
1.0	10 400	0.075	0.679
	22 800	0.067	0.697

TABLE 2. Parameters corresponding to the power-law evolution of standard deviations of the Gaussian curve fits applied to the θ_{rms} profiles: $\sigma_{rms}/h = Ax^m$.

Tavoularis (1989) show that $n_\theta \approx -0.85$ 'near the source' (i.e. for $x_\theta/M \leqslant 10$) and that $n_\theta \approx -1.6$ farther downstream.

The standard deviations of the best-fit Gaussian curves to the r.m.s. temperature profiles (σ_{rms}) are plotted as a function of x/h in figure 10 for the different source locations and Reynolds numbers. We observe that the plumes at the lower Reynolds numbers exhibit slightly larger widths, owing to their correspondingly longer advection times. The best fit power laws to these curves (of the form $\sigma_{rms}/h = Ax^m$) are given in table 2.

Note in table 2 that the scaling exponents, m, show no Reynolds-number dependence. They are, however, strongly dependent on the source location, y_s/h. For the source location closest to the wall ($y_s/h = 0.067$), $m \approx 0.44$. For the source located at $y_s/h = 0.17$, m decreases to 0.36. For the source located at the channel centreline, $m \approx 0.69$. (This non-monotonic trend of m in y_s/h is similar to what was observed for the decay rates of the mean peak temperatures.) The initial drop in m may be attributable to the decrease in turbulence intensity with increasing distance from the wall. Except for locations very close to the wall (i.e. for $y^+ < 20$, e.g. Pope 2000, p. 283), the turbulence intensity falls as one progresses from the wall towards the channel centreline (because the production of turbulent kinetic energy is highest at the wall, where the mean velocity gradient is the largest). Therefore, we would expect m to be the largest for near-wall source locations and smallest for a source located on the channel centreline. However, the subsequent rise in m for $y_s/h = 1.0$ may be attributable to the increased flapping of the plume for such a source location. (The latter phenomenon will be confirmed in the next section when examining the PDFs of the temperature fluctuations.) Flapping is less significant for the $y_s/h = 0.067$ and 0.17 source locations, which are in close proximity to the wall. In this respect, the results pertaining to the $y_s/h = 1.0$ source location are closest to Warhaft's (1984) results in homogeneous, isotropic turbulence, where m is roughly 0.75.

The drift of the peak of the r.m.s. profiles is plotted in figure 11 for the two near-wall source locations and two Reynolds numbers. (Because of the underlying symmetries of the present experiment, the r.m.s. profiles for $y_s/h = 1.0$ must be even functions about $y/h = 1$. Therefore, any centreline peak will not drift.) As expected, the drift of the peaks is smaller for the high-Reynolds-number case, where the plume has less time to diffuse outwards. They also exhibit approximate power-law behaviours, with a scaling exponent of 0.6 for $y_s/h = 0.067$ and 0.5 for $y_s/h = 0.17$. The trend is consistent with the fact that the scaling exponent should tend to zero as $y_s/h \to 1$.

Another quantity of interest is the ratio of the (peak) r.m.s. temperature fluctuation to the (peak) mean temperature excess. In the present flow, we have observed that the peaks of the r.m.s. profiles drift, whereas the peaks of the mean profiles remain

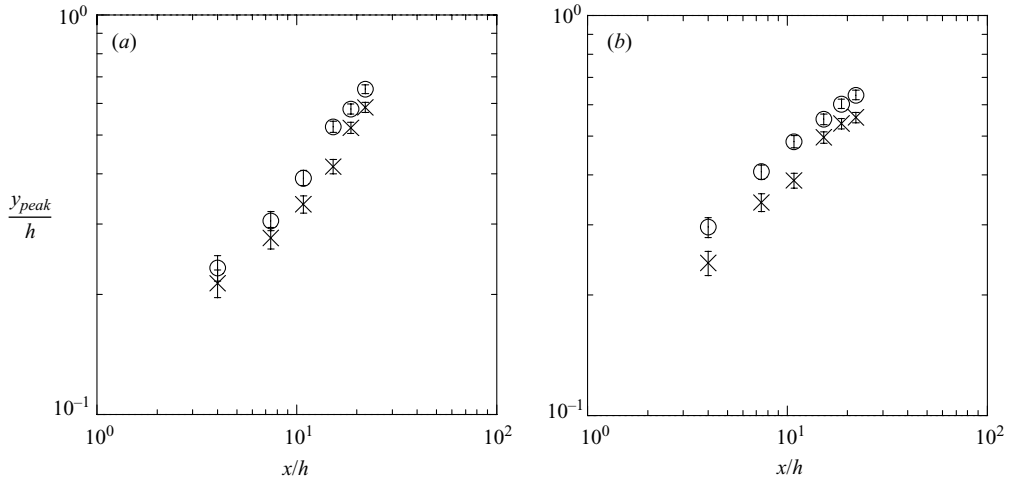

FIGURE 11. The downstream evolution of the transverse location of the peak of the r.m.s. temperature profiles for both Reynolds numbers. (*a*) $y_s/h = 0.067$. (*b*) $y_s/h = 0.17$. ○, $Re = 10\,400$; ×, $Re = 22\,800$.

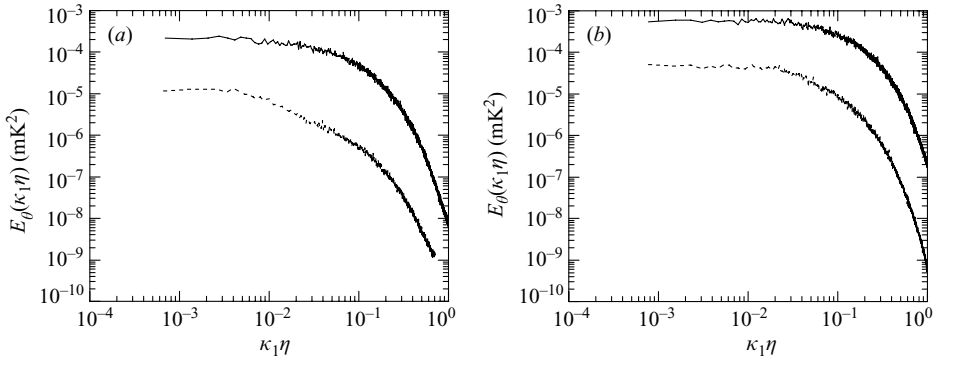

FIGURE 12. Typical power spectra of the temperature fluctuations. Solid line: $x/h = 4.0$. Dashed line: $x/h = 18.6$. (*a*) $y_s/h = y/h = 0.17$. (*b*) $y_s/h = y/h = 1.0$.

relatively fixed. Therefore, calculating such a ratio may not be sensible for the $y_s/h = 0.067$ and 0.17 source locations. However, both the mean and r.m.s. profiles peak at the same location ($y/h = 1.0$) for centreline source locations. For our data, we find that $\theta_{rms\text{–}peak}/\Delta T_{peak}$ decreases monotonically from 1.75 ± 0.1 (at $x/h = 4.0$) to 0.8 ± 0.1 (at $x/h = 18.6$). However, no conclusions regarding asymptotic values can be made. We can remark that the present results are larger than what has been observed in homogeneous flows (Warhaft 1984; Karnik & Tavoularis 1989) and fall within the wide range of observed values in inhomogeneous flows. For example, in the turbulent-boundary-layer work of Fackrell & Robins (1982), the maximum value of this ratio was in the range 1.3 to 5, with larger values associated with smaller (point) source sizes (see Chatwin & Sullivan 1979; Durbin 1980; Sawford & Hunt 1986; Thomson 1990). In fully developed turbulent channel flow, Vrieling & Nieuwstadt (2003) observed a maximum value of $\theta_{rms\text{-}peak}/\Delta T_{peak}$ equal to 0.8 at $x/h = 8$.

Lastly, figure 12 presents typical spectra of the scalar field. Though the spectra were calculated for all the cases studied herein, they generally added little insight to the evolution of the fluctuating scalar field. One noteworthy observation was

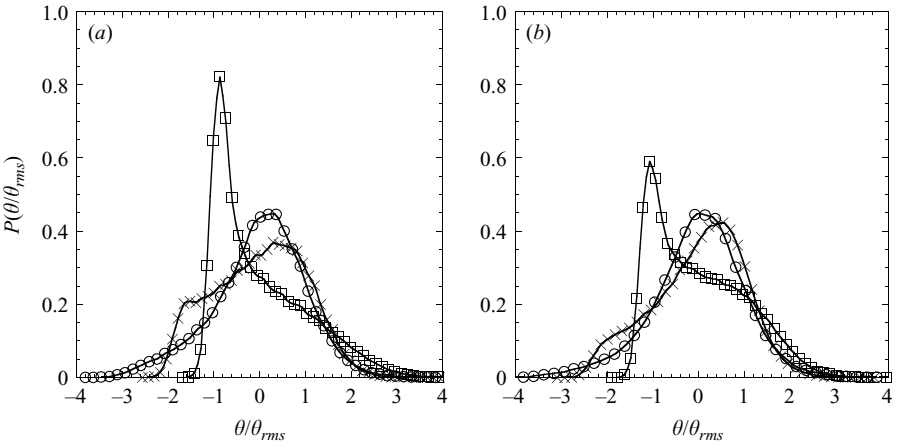

FIGURE 13. PDFs of the temperature fluctuations at $x/h = 7.4$ for $y_s/h = 0.067$. (*a*) $Re = 10\,400$. (*b*) $Re = 22\,800$. ○, $y/h = 0.067$; ×, $y/h = 0.17$; □, $y/h = 0.33$.

that, with the exception of the smallest downstream distances, the spectra exhibited approximate κ_1^{-1} scaling ranges (which were more clearly defined for the near-wall source locations). Such results are reminiscent of those of Villermaux, Innocenti & Duplat (2001), who demonstrated that a κ_1^{-1} scaling results when a scalar whose distribution is intermittent (e.g. from the flapping of the plume) is injected in the inertial range of scales and subject to a fixed stretching rate.

4.3. *Temperature probability density functions*

The statistical distribution of the scalar fluctuations is investigated in this section by considering the probability density functions (PDFs) of the temperature field.

When a scalar is introduced into a turbulent flow at small scales (as is the case in the present work), the temperature fluctuations are produced by two mechanisms. One is the internal turbulent structure of the thermal plume itself. The second is the bulk flapping of the plume, where the instantaneous plume is moved from side to side by the large eddies. The flapping results in a meandering profile of the plume downstream from the source (for the locations where the plume width is smaller than the largest eddies). This manifests itself in the PDF by a spike at a temperature corresponding to that of the cold fluid (for measurement locations that can fall outside of the flapping plume).

PDFs of the temperature fluctuations for different transverse (y) locations are shown in figure 13 at a downstream position of $x/h = 7.4$ for both Reynolds numbers. In this figure, the source location is $y_s/h = 0.067$. Here, the near-wall PDFs are found to be better mixed than those measured farther away from the wall – they are more Gaussian in shape than the PDF measured at $y/h = 0.33$, which exhibits a spike at the corresponding cold fluid temperature. In addition, as the Reynolds number is increased, the near-wall PDFs become even better mixed. For $Re = 22\,800$, the PDF at $y/h = 0.17$ becomes less skewed, more Gaussian in shape and similar to that measured at $y/h = 0.067$. At the higher Reynolds number, the spike of the PDF measured at $y/h = 0.33$ drops from 0.8 to 0.6. This tendency results from the increased mixing associated with higher Reynolds numbers and is more significant than the fact that the scalar has had less time to mix (because of the faster advection).

Analogous measurements for a source location of $y_s/h = 0.17$ are given in figure 14. Here, similar results are obtained – the PDF evolves from an approximately Gaussian

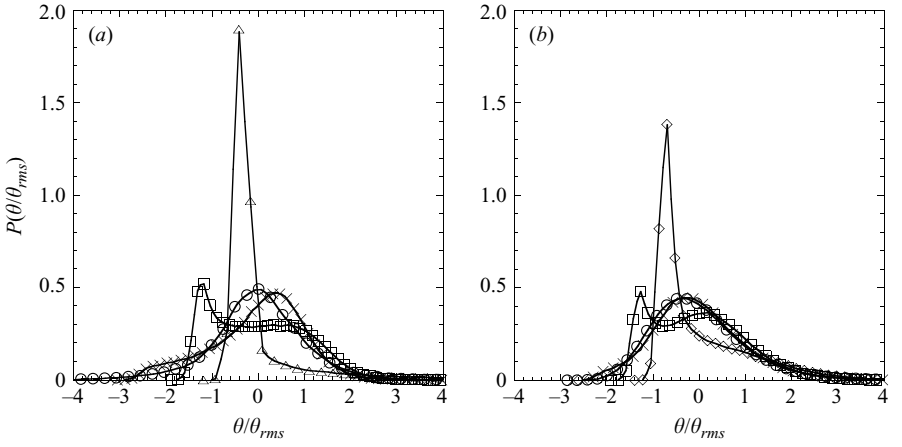

FIGURE 14. PDFs of the temperature fluctuations at $x/h = 7.4$ for $y_s/h = 0.17$. (*a*) $Re = 10\,400$. (*b*) $Re = 22\,800$. ○, $y/h = 0.067$; ×, $y/h = 0.17$; □, $y/h = 0.33$; ◇, $y/h = 0.50$; △, $y/h = 0.67$.

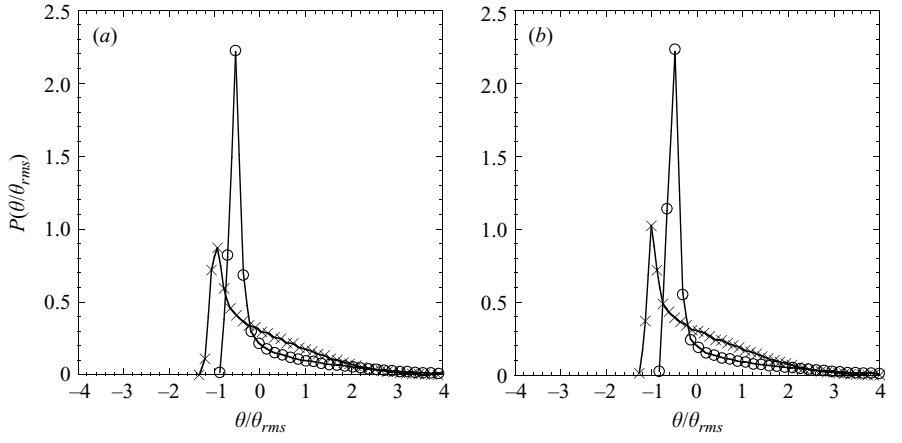

FIGURE 15. PDFs of the temperature fluctuations at $x/h = 7.4$ for $y_s/h = 1.0$. (*a*) $Re = 10\,400$. (*b*) $Re = 22\,800$. ○, $y/h = 0.8$; ×, $y/h = 1.0$.

shape near the wall to a skewed spiked shape as the centre of the channel is approached. As before, increasing the Reynolds number improves the mixing in the flow. Note that the location of the cold fluid spike changes. This results from the fact that the mean temperature changes in the transverse (y) direction. When the PDFs are plotted dimensionally versus the total temperature, $\Delta T + \theta$ (not shown), the locations of the cold spikes all align at T_∞.

PDFs of the thermal plume emanating from a source located at the channel centreline ($y_s/h = 1.0$) are shown at $x/h = 7.4$ in figure 15. For all transverse locations (even $y/h = 1.0$ – directly behind the source), the PDF is spiked and positively skewed, implying that flapping of the thermal plume plays a dominant role in the dispersion of the scalar at this central source location.

The downstream evolution of the PDFs are shown in figure 16. All measurements are for transverse locations that are downstream of the source (i.e. $y = y_{source}$). As the downstream distance increases, the PDF becomes better mixed for all source locations and Reynolds numbers. As the source is located farther from the

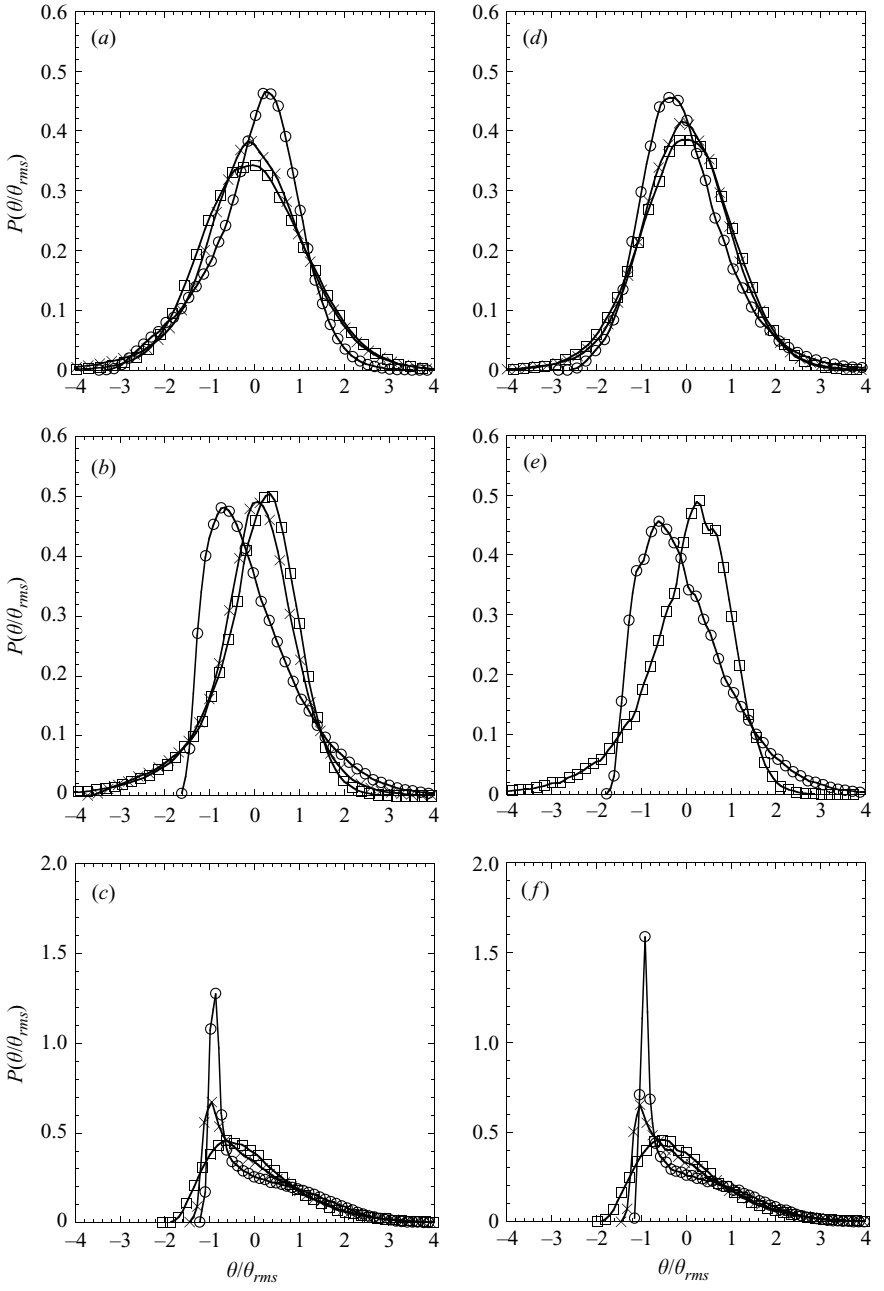

FIGURE 16. The downstream evolution of the PDFs of the temperature fluctuations. The transverse position in each figure is behind the source location (i.e. $y = y_s$). (*a*)–(*c*) correspond to $Re = 10\,400$. (*d*)–(*f*) correspond to $Re = 22\,800$. (*a*), (*d*) $y_s/h = 0.067$. (*b*), (*e*) $y_s/h = 0.17$. (*c*), (*f*) $y_s/h = 1.0$. ○, $x/h = 4.0$; ×, $x/h = 10.8$; □, $x/h = 22.0$.

wall, the PDF is more positively skewed, indicating that the near-wall source locations mix the scalar better in the initial stages of the plume. Such a result is consistent with the larger turbulence intensity near the wall and increased flapping of the plume for the centreline source location.

For many combinations of position (x/h, y/h) and source location (y_s/h), the PDFs exhibit a spiked, positively skewed shape. Other measurements (e.g. Fackrell & Robins 1982; Villermaux *et al.* 1998; Brethouwer *et al.* 1999) have shown PDFs that were described well by exponential curves. Plotting the present results in a log–linear form (where an exponential appears as a straight line) indicates that the above mentioned PDFs are not inconsistent with these results. However, we remark that the quality of the (exponential) fit to the PDFs is inferior to those observed in Villermaux *et al.* (1998). In log-linear coordinates, the exponential tail of the PDF often displays a slight concave-down 'hump'. Such a phenomenon may be a remnant of the peak of the PDF pertaining to samples that are measured when the probe is inside the plume (as opposed to the peak at the cold fluid temperature. See, for example, the bimodal PDF for $y/h = 0.33$ in figure 14(*b*), which clearly shows both peaks.) The existence of the hump may derive from the bounded nature of the present flow that limits the flapping of the plume.

Some insight into the mixing process can be obtained by considering the transverse r.m.s. profiles of the previous section in conjunction with the PDFs. If we consider the shapes of the PDFs at the locations where the r.m.s. profiles peak, the PDFs are found to exhibit similar shapes. This shape has two smaller spikes – one at the cold-fluid temperature and another at a temperature corresponding to the hotter fluid (i.e. the plume). For an example of this (see figure 14*b*) the PDF at $y/h = 0.33$ for $y_s/h = 0.17$, $x/h = 7.4$ and $Re = 22\,800$. (Figure 8 shows that the corresponding r.m.s. profile peak is in the vicinity of $y/h \approx 0.35$. This was verified for other cases not shown here.) The implication to be drawn from this is that the r.m.s. fluctuations contain an important contribution from the flapping of the thermal plume and do not exclusively result from the internal structure of the plume itself.

The tendency towards strongly positively-skewed PDFs away from the centres of the plumes is evident in figure 17, where transverse skewness profiles are plotted. Results are presented for the three source positions, the two Reynolds numbers and selected downstream distances. Near the centres of the plumes, the PDFs of θ are relatively symmetric and therefore have skewnesses around zero. However, as the edges of the plumes are approached, the PDFs become positively skewed and their skewness increases. Very far away from the sources locations (and therefore centres of the plume), the skewness falls to zero outside the plume. As the downstream distance increases, the PDFs become better mixed and the skewnesses consequently drop. With respect to the skewness profiles corresponding to near-wall source locations, it is of interest to note that the near-wall skewness falls to negative values for large enough downstream distances. This indicates that such locations are most often inside the plume and experience occasional bursts of cold fluid – the opposite of what occurs on the edges of the plume. However, consistent with the results of Brethouwer *et al.* (1999), this is not the case for the plumes emanating from centreline source locations, which have positive skewnesses for all transverse and downstream locations.

4.4. *Velocity-temperature correlations*

Results for specific combinations of source location (y_s/h), downstream position (x/h) and Reynolds number are given below. For results pertaining to combinations not presented herein, the reader is referred to Lavertu (2002).

The correlation coefficients of (i) u and θ and (ii) v and θ are defined by:

$$\rho_{u\theta} \equiv \frac{\langle u\theta \rangle}{u_{rms}\theta_{rms}} \tag{4.1}$$

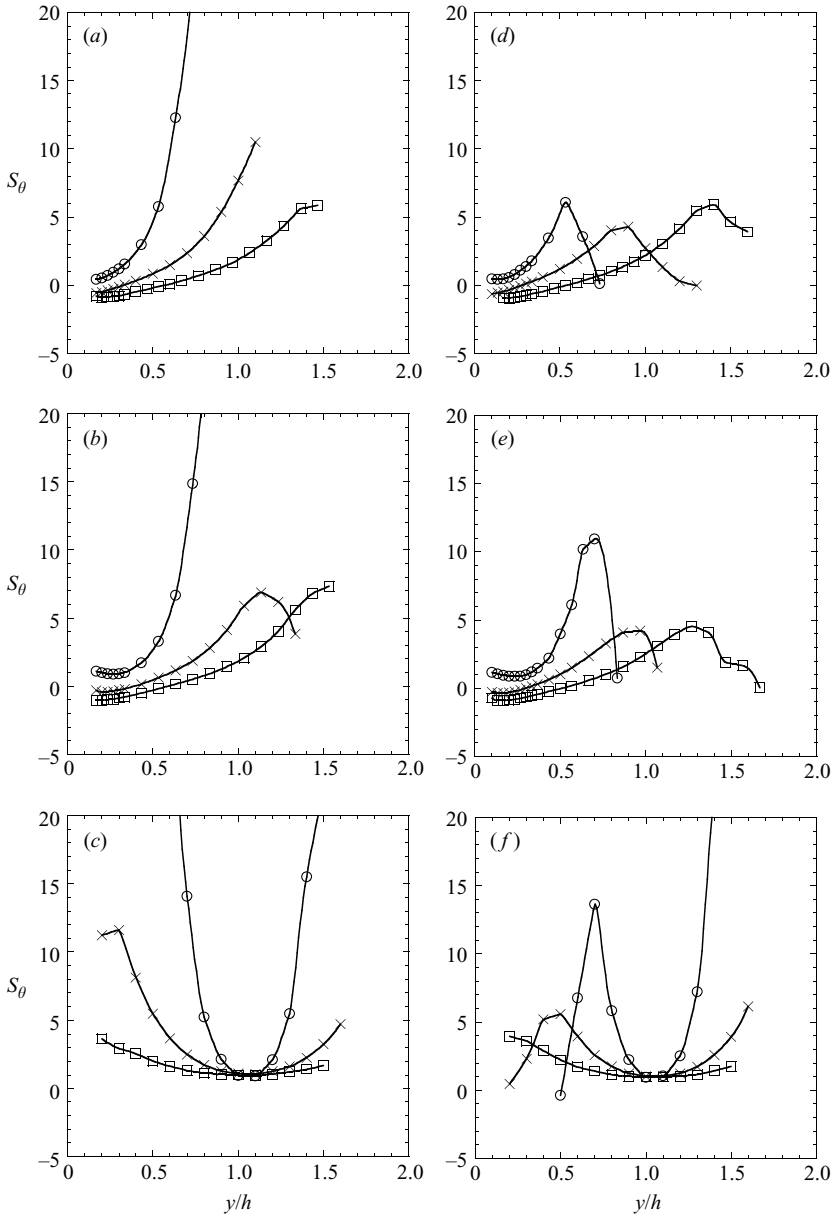

FIGURE 17. Transverse profiles of the skewness of the temperature fluctuations at different downstream locations for the three source locations and the two Reynolds numbers. (*a*)–(*c*) correspond to $Re = 10\,400$. (*d*)–(*f*) correspond to $Re = 22\,800$. (*a*), (*d*) $y_s/h = 0.067$. (*b*), (*e*), $y_s/h = 0.17$. (*c*), (*f*) $y_s/h = 1.0$. ○, $x/h = 4.0$; ×, $x/h = 10.8$; □, $x/h = 22.0$.

and

$$\rho_{v\theta} \equiv \frac{\langle v\theta \rangle}{v_{rms}\theta_{rms}}. \tag{4.2}$$

$\rho_{u\theta}$ and $\rho_{v\theta}$ are presented in figure 18 at $x/h = 7.4$ and $Re = 10\,400$ for the three source locations. They represent the non-dimensional longitudinal and transverse

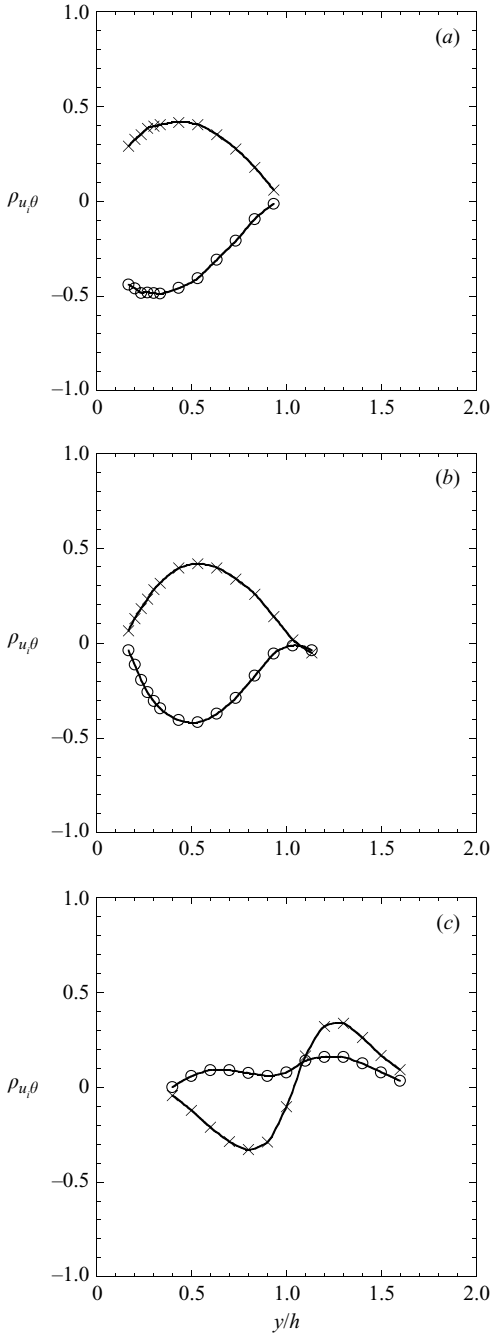

FIGURE 18. Transverse profiles of the correlation coefficients of velocity and temperature, $\rho_{u_i\theta}$. ○, $\rho_{u\theta}$; ×, $\rho_{v\theta}$. (*a*) $y_s/h = 0.067$. (*b*) $y_s/h = 0.17$. (*c*) $y_s/h = 1.0$. $x/h = 7.4$. $Re = 10\,400$.

turbulent heat fluxes, respectively. For the off-centreline source locations, $\rho_{u\theta}$ and $\rho_{v\theta}$ are opposite in sign because of the negative correlation between u and v in this region of the flow. As necessitated by the underlying symmetries, $\rho_{u\theta}$ exhibits even (and $\rho_{v\theta}$ exhibits odd) symmetry about the channel centreline for $y_s/h = 1.0$.

The Reynolds number and downstream distance from the source do not change the overall shape of the heat flux profiles significantly. With increasing Reynolds number, the profiles become slightly thinner, consistent with the profiles in the previous sections. As the downstream distance is increased, the profiles widen, as expected. For the near-wall source locations, $\rho_{u\theta}$ and $\rho_{v\theta}$ peaked at values of -0.4 to -0.5 and 0.4 to 0.5, respectively, with a slight tendency towards larger magnitudes for larger x/h. For the centreline source locations, the peaks of $\rho_{u\theta}$ increased from approximately 0 to 0.4 (opposite to the results of Brethouwer *et al.* 1999) and the peaks of $\rho_{v\theta}$ decreased from approximately 0.4 to 0.3 when x/h was increased. The results for near-wall sources are (i) similar to those of Fackrell & Robins (1982), Raupach & Legg (1983) and El Kabiri *et al.* (1998) in turbulent boundary layers and (ii) significantly different from those for $y_s/h = 1.0$. In addition, the profiles of the turbulent heat fluxes are significantly different from the results obtained in homogeneous flows (e.g. Karnik & Tavoularis 1989) owing to the presence of the wall and the different underlying symmetries of the two flows.

The turbulent transport of scalar variance by velocity fluctuations, $\langle\theta^2 u_i\rangle$, is given in figure 19 at $x/h = 7.4$ and both Reynolds numbers for the three source locations. The longitudinal and transverse transport terms are non-dimensionalized as follows:

$$\langle\theta^2 u\rangle_{ND} \equiv \frac{\langle\theta^2 u\rangle}{\langle\theta^2\rangle u_{rms}} \tag{4.3}$$

and

$$\langle\theta^2 v\rangle_{ND} \equiv \frac{\langle\theta^2 v\rangle}{\langle\theta^2\rangle v_{rms}}. \tag{4.4}$$

It is worth noting that the non-dimensionalized quantities are not correlation coefficients and are therefore not bounded by ± 1. (This will be relevant shortly.) As with the turbulent heat fluxes, the near-wall source locations produce results similar to those in turbulent boundary layers, but significantly different from those corresponding to the centreline source location.

In studying figure 19, there appears to be a significant Reynolds-number dependence – especially for the near-wall source locations. As the Reynolds number increases, the peaks of the non-dimensional scalar variance transport decrease in magnitude. However, the shapes of the profiles remain similar. This decrease is due to the non-dimensionalization. Considering θ^2 to be a variable in and of itself, a correlation coefficient can be defined as follows:

$$\rho_{\theta^2 u_i} \equiv \frac{\langle\theta^2 u_i\rangle}{(\theta^2)_{rms} u_{irms}} = \frac{\langle\theta^2 u_i\rangle}{(\sqrt{K(\theta)-1})\langle\theta^2\rangle u_{irms}}, \tag{4.5}$$

noting that the r.m.s. of θ^2 (i.e. $(\theta^2)_{rms}$) can be re-written as:

$$(\theta^2)_{rms} \equiv \langle(\theta^2 - \langle\theta^2\rangle)^2\rangle^{1/2} = \langle\theta^4\rangle^{1/2} - \langle\theta^2\rangle = (\sqrt{K(\theta)-1})\langle\theta^2\rangle, \tag{4.6}$$

where the kurtosis of the scalar is defined as:

$$K(\theta) \equiv \frac{\langle\theta^4\rangle}{\langle\theta^2\rangle^2}. \tag{4.7}$$

Given that the correlation coefficient $\rho_{\theta^2 u_i}$ must be bounded by ± 1, the non-dimensionalized scalar variance turbulent transport terms $\langle\theta^2 u\rangle_{ND}$ and $\langle\theta^2 v\rangle_{ND}$ must be bounded by $\pm(\sqrt{K(\theta)-1})$, cf. equations (4.3) – (4.5). The ratio of $(\sqrt{K(\theta)-1})$ at $Re = 10\,400$ to $(\sqrt{K(\theta)-1})$ at $Re = 22\,800$ (at the locations of the peaks of $\langle\theta^2 v\rangle$ for

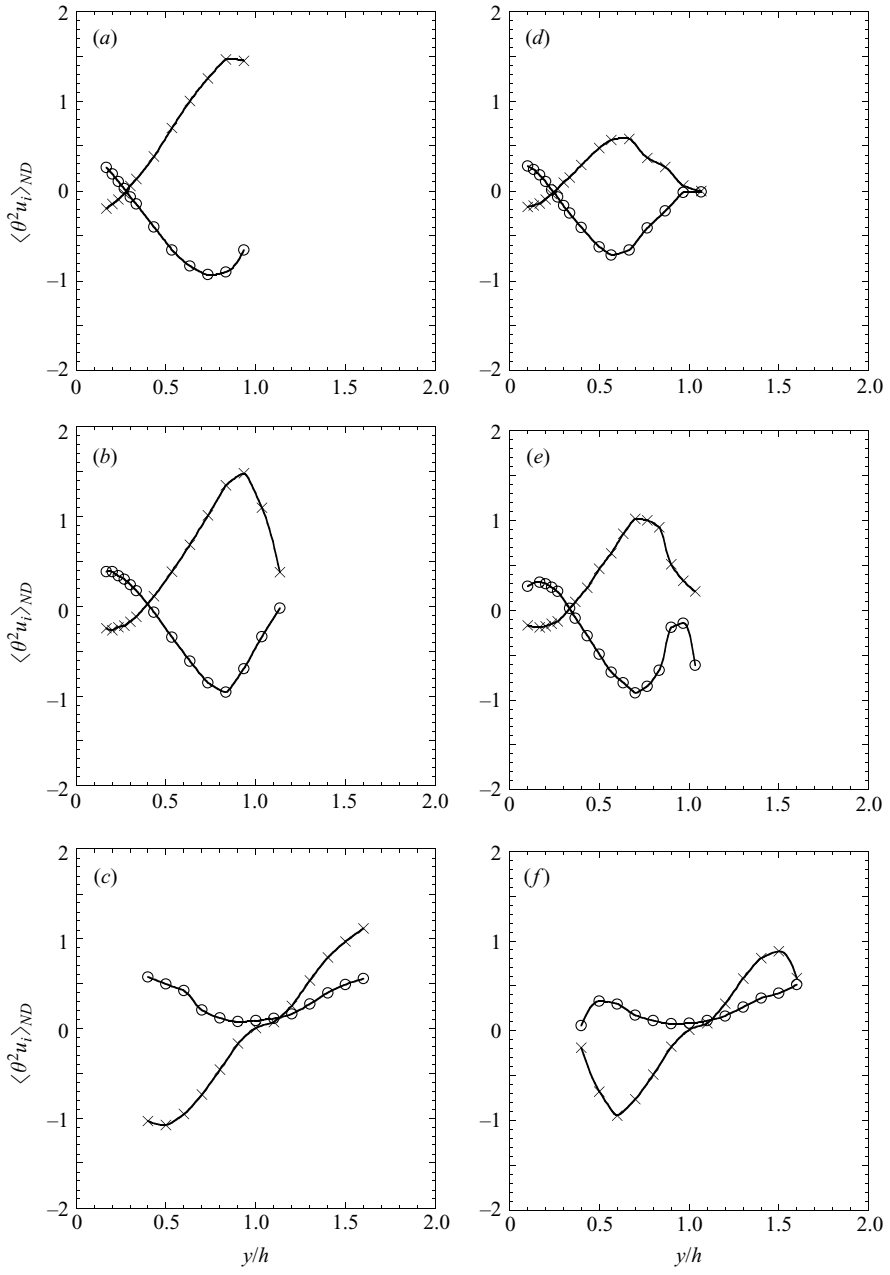

FIGURE 19. Transverse profiles of the non-dimensionalized turbulent transport of scalar variance, $\langle\theta^2 u_i\rangle_{ND}$. ○, $\langle\theta^2 u\rangle_{ND}$; ×, $\langle\theta^2 v\rangle_{ND}$. (*a*)–(*c*) correspond to $Re = 10\,400$. (*d*)–(*f*) correspond to $Re = 22\,800$. (*a*), (*d*) $y_s/h = 0.067$. (*b*), (*e*) $y_s/h = 0.17$. (*c*), (*f*) $y_s/h = 1.0$.

$y_s/h = 0.067$ and $x/h = 7.4$) is 2.2. This is not inconsistent with the ratio of the peaks of $\langle\theta^2 v\rangle_{ND}$, and suggests that the non-dimensionalization is presumably the source of the apparent Reynolds-number dependence. (As for the mean, r.m.s. and skewness profiles, the variation in the kurtosis of the scalar field with Reynolds number is dominated by the narrowing of the plume width at higher advection velocities.) To

remove the apparent Reynolds-number dependence, the scalar variance turbulent transport could be non-dimensionalized following (4.5). This, however, is not the standard convention and is the reason it was not used. Nevertheless, this shows the effect of the PDF shape and its Reynolds-number dependence on the transport of θ^2.

As x/h increases (not shown), the turbulent scalar variance transport profiles broaden, as expected. For the non-centreline source locations, the peaks of both $\langle\theta^2 u\rangle_{ND}$ and $\langle\theta^2 v\rangle_{ND}$ decrease in magnitude with downstream distance for both Reynolds numbers. At $x/h = 7.4$, the peaks of both profiles occur at the same transverse location. Although the widths of both profiles are the same farther downstream, the peak of $\langle\theta^2 u\rangle_{ND}$ does not drift as much as that of $\langle\theta^2 v\rangle_{ND}$. For the centreline source location, the peaks of $\langle\theta^2 u\rangle_{ND}$ increased in the downstream distance, whereas the peaks of $\langle\theta^2 v\rangle_{ND}$ decreased.

The last velocity–temperature correlation to be considered is the transport of turbulent heat flux by turbulent velocity fluctuations, $\langle u^2\theta\rangle$ and $\langle v^2\theta\rangle$, given in figure 20 at $x/h = 7.4$ and $Re = 10\,400$ for the three source locations. The longitudinal and transverse terms are non-dimensionalized as follows:

$$\langle u^2\theta\rangle_{ND} \equiv \frac{\langle u^2\theta\rangle}{\langle u^2\rangle\theta_{rms}} \tag{4.8}$$

and

$$\langle v^2\theta\rangle_{ND} \equiv \frac{\langle v^2\theta\rangle}{\langle v^2\rangle\theta_{rms}}. \tag{4.9}$$

For the two cases corresponding to near-wall sources, the profiles are similar – negative close to the wall, becoming positive away from the wall and returning to zero far away from the wall. For the centreline source location, both profiles exhibit even symmetry about the centreline, as required. The Reynolds-number dependence of the (turbulent) transport of turbulent heat flux is limited to a slight thinning of the profile widths at higher Re. No spurious Reynolds-number dependence is observed for these triple correlations as was observed for $\langle\theta^2 u_i\rangle$ given that the present non-dimensionalization depends on $K(u)$ and $K(v)$ (and not $K(\theta)$), which are more constant because they do not depend on the width of the thermal plume. Lastly, the downstream dependence of $\langle u^2\theta\rangle_{ND}$ and $\langle v^2\theta\rangle_{ND}$ (not shown) is as expected – the profiles broaden as x/h increases. There is a slight tendency towards higher peaks with increasing x/h for the near-wall source locations.

5. Conclusions and discussion

The mixing of a scalar (temperature) emitted from a concentrated line source in fully developed, high-aspect-ratio channel flow was studied. Results treating the (i) mean temperature field, (ii) fluctuating temperature field, (iii) probability density functions of the temperature fluctuations and (iv) velocity–temperature correlations were presented. Three source locations ($y_s/h = 0.067$, 0.17 and 1.0) and two Reynolds numbers ($Re = 10\,400$ and $22\,800$) were considered. Statistics were presented for $4.0 \leqslant x/h \leqslant 22.0$. This range of downstream distances is beyond the molecular diffusive range. A significant turbulent diffusive range is not expected herein because of the bounded nature of the flow and the consequent inability of the plume to be wider than the largest eddies of the flow.

The mean temperature excess profiles are found to be described well by truncated Gaussian distributions. The centres of the profiles remain relatively fixed at a transverse location downstream of the source. The downstream evolution of the

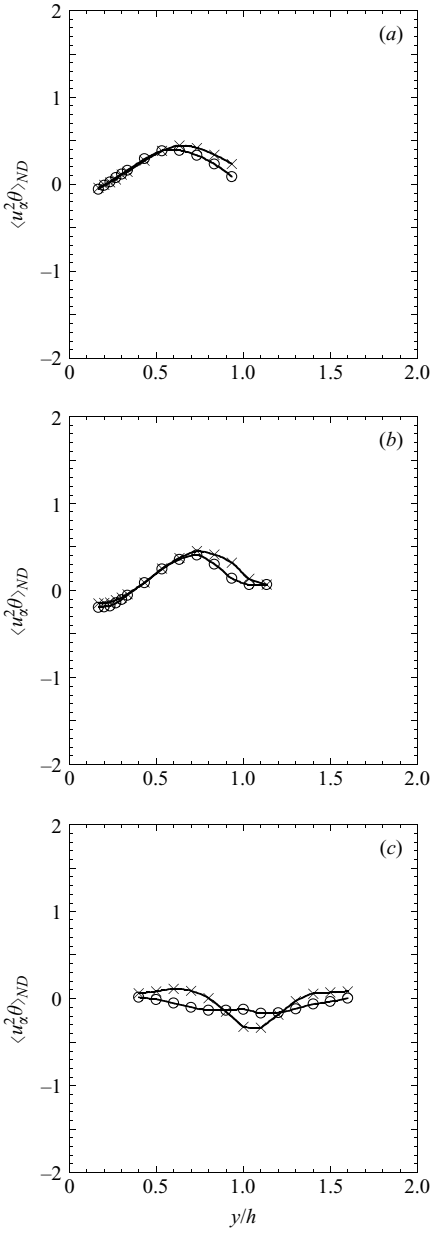

FIGURE 20. Transverse profiles of the non-dimensionalized transport of turbulent heat flux by turbulent velocity fluctuations, $\langle u_\alpha^2\theta\rangle_{ND}$. ○, $\langle u^2\theta\rangle_{ND}$; ×, $\langle v^2\theta\rangle_{ND}$. (*a*) $y_s/h = 0.067$. (*b*) $y_s/h = 0.17$. (*c*) $y_s/h = 1.0$. $x/h = 7.4$. $Re = 10\,400$.

peak temperature excess can be approximated (over the downstream distances under consideration) by a power law with a decay exponent, n, in the range −0.5 to −0.7. The value of n depends on the transverse location of the source (y_s), with the fastest decay occurring for the source located at $y_s/h = 0.067$ and the slowest decay occurring for $y_s/h = 0.17$. The standard deviations of the profiles – a measure of the profile width – grow at a rate that decreases with downstream distance, thus exhibiting the effects of the inhomogeneous, bounded nature of the flow.

Like the mean temperature excess profiles, the r.m.s. temperature fluctuation profiles are described well by truncated Gaussian distributions for the downstream distances considered herein. However, unlike the mean profiles, the peaks of the r.m.s. profiles drift towards the channel centreline (for off-centreline source locations). The downstream decay of the peak r.m.s. temperature follows an approximate power-law behaviour with a decay exponent of approximately -1. Similar to the mean profiles, the growth rate of the standard deviations of the r.m.s. profiles was a non-monotonic function of the source location.

The PDFs of the scalar fluctuations exhibited strong dependencies on the source location, the downstream position and the transverse position. For the near-wall source locations, the PDF of the scalar field evolves from a quasi-Gaussian distribution near the wall to a strongly positively-skewed PDF with a large spike at the cold fluid temperature in the tail of the mean profile (i.e. far from the wall). In addition, increasing the Reynolds number was found to improve the mixing undergone by the scalar. Given that increasing the Reynolds number (by increasing the mean velocity) has two opposite effects – increasing the turbulent Reynolds number (and therefore the mixing) versus decreasing the amount of time for which the scalar is mixed (due to the faster advection) – such a result is not evident *a priori*. For source locations at the centreline, the scalar PDF is initially spiked and positively-skewed for all transverse positions. This indicates that the flapping of the plume plays an important role for that source location. As would be expected, the PDFs become better mixed (for all source locations and Reynolds numbers) as the downstream distance increases.

Lastly, velocity–temperature correlations were measured. The profiles of all the correlations presented herein are strongly dependent on the source location. The profiles of the correlation coefficients of the (longitudinal and transverse) velocity and temperature fluctuations are relatively independent of the Reynolds number. All profiles broaden with increasing x/h. For the two near-wall source locations, $\rho_{u\theta}$ and $\rho_{v\theta}$ peak at values of -0.4 to -0.5 and 0.4 to 0.5, respectively, with a slight tendency towards larger magnitudes at larger x/h. For the centreline source locations, $\rho_{u\theta}$ and $\rho_{v\theta}$ exhibit symmetric and anti-symmetric profiles about the centreline, as required. In this case, the profiles broaden, the peaks of $\rho_{u\theta}$ increase from approximately 0 to 0.4 and the peaks of $\rho_{v\theta}$ decrease from approximately 0.4 to 0.3 with increasing x/h.

The turbulent transport of scalar variance exhibits profiles that broaden and peaks that decrease in magnitude with increasing x/h for the near-wall source locations. For the centreline source location, the peaks of $\langle\theta^2 u\rangle_{ND}$ increase in the downstream distance, whereas the peaks of $\langle\theta^2 v\rangle_{ND}$ decrease in that same direction. There appeared to be a Reynolds-number dependence of $\langle\theta^2 u_i\rangle_{ND}$ – especially for the near-wall source locations. However, this dependence was attributed to the non-dimensionalization, which is sensitive to the shape of the scalar plume, which narrows at the higher Reynolds number.

The transport of turbulent heat flux by turbulent velocity fluctuations, $\langle u_\alpha^2\theta\rangle_{ND}$ shows no significant Reynolds-number dependence other than a slight narrowing of the profiles. The profiles widen as the plume evolves in the downstream direction and the peak of the profiles for the near-wall source locations tends to slightly larger values with increasing x/h.

Given that (i) the motivation for the present work was the explicit determination of the effect of inhomogeneity in the flow on the dispersion of a scalar within it, and (ii) scalar dispersion in a turbulent boundary layer has received much attention in the past (whereas scalar dispersion in channel flow has not), an explicit comparison

of the scalar mixing process in the two flows is required. Recall that their principal differences are (i) the existence of a weak longitudinal inhomogeneity in boundary layers (which is absent in channel flow), and (ii) the different nature of their outer flows. The importance of the former is probably smaller than that of the latter, which should be significant outside of the inner layer.

Strong differences between the dispersion within turbulent boundary layers and the present work should be anticipated for scalar statistics resulting from the $y_s/h = 1.0$ source, which is located in the outer region as far as possible from the wall. Some differences may be observed for the $y_s/h = 0.17$ source location, which is located outside the inner layer, though still in the log-law region (as defined by Pope 2000, p. 275). The fewest differences should be expected for the $y_s/h = 0.067$ source location statistics because the source is located within the inner layer. Nevertheless, differences remain possible once the plume has diffused outside the inner layer, which occurs very rapidly (see figure 5).

Some of the differences (and similarities) have already been reported in § 4. For example, the peaks of the r.m.s. profiles (figure 8) are found to drift towards the centreline for the two near-wall source locations, but the peak of the r.m.s. profile remained stationary when the source was located at $y_s/h = 1.0$. The latter is merely a consequence of the underlying symmetry of channel flow. However, this lack of an analogous symmetry in turbulent boundary layers (that derives from the different geometry of the flow) is precisely what causes the two flows to have different outer layers. In comparing the data from the $y_s/h = 0.17$ source location and that of the elevated line source of Fackrell & Robins (1982) (for $y_s/H = 0.19$, where H is their boundary-layer thickness), the displacement of the peaks of the r.m.s. profiles appear similar, though the data of Fackrell & Robins (1982) only extend to $x/H = 6.52$ (where $y_{peak}/H = 0.3$, similar to figure 11*b*). As their plume disperses farther downstream (and consequently farther away from the wall, deeper into the outer layer), larger differences could be expected. For example, the r.m.s. profiles of El Kabiri *et al.* (1998) peak at $y_{peak}/\Delta_o = 0.6$ at a downstream distance of $x/\Delta_o = 10.4$ for $y_s/\Delta_o = 0.3$ (Δ_o is their boundary-layer thickness.) Nevertheless, given the differences in Reynolds numbers, source locations, and lack of a Lagrangian rescaling of the downstream distances, strong conclusions should be avoided.

Furthermore, for the larger downstream distances, the r.m.s. profiles behind the centreline source become sub-Gaussian (see figure 8*c*, *f*). This is not the case for the r.m.s. profiles behind the two near-wall sources, which are approximated very well by truncated Gaussian distributions for all x/h. To our knowledge, such sub-Gaussian scalar r.m.s. profiles have not been observed in turbulent boundary layers. We conjecture that such a characteristic arises from the growth of the tails of the r.m.s. profile being impeded by the walls. Following this train of thought, we might expect that at larger x/h than measured herein, the r.m.s. profiles emanating from a near-wall sources would also become sub-Gaussian because their tails will begin to be affected by the far ($y/h = 2.0$) wall. Given that the tails must travel twice as far to 'encounter' a wall (i.e. $\sim 2h$ versus h for a centreline source), such an observation would not occur until farther downstream.

In the same vein, the observed non-monotonic trend (in y_s/h) of the scaling exponents of σ_{rms}/h as a function of x/h (m – see table 2) is almost certainly related to the outer-layer flow in a channel. Excepting for locations very close to the wall, the turbulence intensity decreases with increasing distance from the wall (as is also the case in turbulent boundary layers). This is consistent with σ_{rms}/h growing more rapidly for $y_s/h = 0.067$ than for $y_s/h = 0.17$. However, this trend is counteracted – presumably

by the flapping of the plume, which is most significant for centreline sources – causing m to be maximal for $y_s/h = 1.0$. The difference between near-wall and outer-layer source locations in plumes dispersing in turbulent boundary layers is not expected to be as significant as the difference between near-wall and centreline plumes in channel flow.

With regard to velocity–temperature correlations, the present results for $y_s/h = 0.067$ and $y_s/h = 0.17$ are similar to those observed in turbulent boundary layers (e.g. Raupach & Legg 1983). The correlation coefficients (i) are approximately zero at $y = y_s$ (in conjunction with gradient transport theory, given that the mean temperature profiles peak at y_s), (ii) increase in magnitude above the source (peaking with magnitudes of 0.4–0.5), and (iii) subsequently fall to zero far above the source. Profiles of $\rho_{u_i\theta}$ like those in figure 18(c) for a centreline source have not been observed in turbulent boundary layers and would be unlikely to occur given its different geometry and outer flow. Similar results and arguments can be drawn for the third-order velocity–temperature correlations (see, for example, El Kabiri *et al.* 1998 for results in a turbulent boundary layer).

Finally, it is tempting to relate the results of § 4 to the dynamics of the coherent structures in wall-bounded flows. (See, for example, Robinson 1991 for an overview†.) Coherent structures are of capital importance to the production of turbulent kinetic energy in the near-wall region ($y^+ < 100$). Here, the dominant structures are pairs of elongated counter-rotating vortices (or rolls) whose axes are aligned with the mean flow direction. Given the presence of a (wall-normal) mean velocity gradient, they engender low-speed streaks of low-momentum fluid very close to the wall ($y^+ < 10$). The streaks induce inflection points in the mean velocity profile, leading to flow instabilities, which result in intermittent intense outward ejections of the low-speed fluid away from the wall, subsequently breaking down into small-scale turbulence. To balance the ejections, high-speed fluid rushes towards the wall in what are called sweeps. The rolls then form again to create a quasi-cyclic 'bursting' process.

The above phenomena are alternatively interpreted in terms of horseshoe or hairpin vortices. The long quasi-streamwise tails of these structures cause the streaks, whereas the ejections result from the lifting of the hairpin head and pumping up of fluid from in between its legs.

The majority of the production of turbulent kinetic energy results from the ejection and sweeps, which are second and fourth $u - v$ quadrant motions (see Wallace, Eckelmann & Brodkey 1972; Willmarth & Lu 1972). In other words, they correspond to negative Reynolds stress ($uv < 0$) motions, which generate turbulent kinetic energy in the amount $-\langle uv\rangle \partial\langle U\rangle/\partial y$. Given the influence of these structures in the near-wall region on the transport of momentum, they must certainly also affect the transport of scalars therein.

Though the objective of the present work was not the study of the relationship between scalar transport and the dynamics of coherent structures in wall-bounded flows, some of the results may nevertheless lend some insight. For three of the six cases under study ($y_s/h = 0.067$ and $Re = 10\,400$; $y_s/h = 0.067$ and $Re = 22\,800$; $y_s/h = 0.17$ and $Re = 10\,400$), the source location is in the near-wall region ($y_s^+ < 100$). In these instances, the scalar mixing process close to the wall is undoubtedly affected, if not dominated, by the near-wall dynamics.

† Though a significant fraction of the work pertaining to coherent structures in turbulent flow has been undertaken in boundary layers, it is expected that the near-wall dynamics in channel flow and boundary layers should be the same (Holmes, Lumely & Berkooz 1996).

The PDFs of scalar fluctuations emanating from near-wall sources (figures 13 and 14) exhibited a clear tendency towards Gaussian distributions as the measurement location approached the wall. This is symptomatic of intense mixing in the near-wall region, which results from the ejections and sweeps that also cause the turbulent kinetic energy to peak therein. Though we might initially hypothesize that the bursting process might result in a flapping of the plume (which would result in PDFs with spikes at the free-stream temperature), such a phenomenon was not observed. Given that the plume width was already larger than the height of the near-wall region for the downstream positions studied herein, ejections and sweeps could not be expected to 'flap' a plume. Because the ejections and sweeps occur over distances smaller than the plume width, they serve instead to mix the plume intensely, which agrees with the observation of Gaussian PDFs close to the wall. Should PDFs of scalars released from near-wall sources be studied for small downstream distances (such that the plume width was significantly smaller than the height of the near-wall region), flapping of the plume (and the subsequent spiked PDFs) could be expected.

The relationship between scalar transport and coherent structures in wall-bounded turbulent flows is perhaps best studied by simultaneous velocity and temperature measurements. Thus, the velocity–temperature correlations of §4.4 should be of particular interest. Regrettably, the X–T probe assembly used in this work did not allow measurements to be made below $y/h = 0.17$, thus precluding the measurement of near-wall correlations.

The relationship between the outer and inner regions is not yet clear, though results suggest that though the former affects the latter, it does not control it (Robinson 1991). Furthermore, the nature of coherent structures in the outer layer of wall-bounded flows, especially channel flow, is less well understood. Work in this area is in progress (e.g. Kim & Adrian 1999; Christensen & Adrian 2001; Liu, Adrian & Hanratty 2001) and will hopefully serve to further our understanding of (and therefore our ability to modify, as desired) scalar transport in the outer region of wall-bounded flows.

The authors would like to thank T. Antonakakis, P. Blossey, K. Christensen, E. Costa-Patry, S. Karlsson, J. Lemay, B. Pearson, S. Tavoularis and Z. Warhaft for their help with various aspects of this work. The reviewers are also thanked for their constructive comments. Support was provided by the Natural Sciences and Engineering Research Council of Canada and the Fonds pour la Formation de Chercheurs et l'Aide à la Recherche du Québec.

REFERENCES

Anand, M. S. & Pope, S. B. 1983 Diffusion behind a line source in grid turbulence. In *Proc. 4th Symp. on Turbulent Shear Flows, Karlsruhe, Germany*. Springer.

Bara, B. M., Wilson, D. J. & Zelt, B. W. 1992 Concentration fluctuation profiles from a water channel simulation of a ground-level release. *Atmos. Environ.* **26A**, 1053–1062.

Bernard, P. S. & Rovelstad, A. L. 1994 On the physical accuracy of scalar transport modelling in inhomogeneous turbulence. *Phys. Fluids* **6**, 3093–3108.

Blevins, R. D. 1990 *Flow-Induced Vibrations*, 2nd edn. Krieger.

Brethouwer, G., Boersma, B. J., Pourquié, M. B. J. M. & Nieuwstadt, F. T. M. 1999 Direct numerical simulation of turbulent mixing of a passive scalar in pipe flow. *Eur. J. Mech.* B/*Fluids* **18**, 739–756.

Browne, L. W. B. & Antonia, R. A. 1987 The effect of wire length on temperature statistics in a turbulent wake. *Exps. Fluids*, **5**, 426–428.

Browne, L. W. B., Antonia, R. A. & Chua, L. P. 1989 Calibration of X-probes for turbulent flow measurements. *Exps. Fluids* **7**, 201–208.

Chatwin, P. C. & Sullivan, P. J. 1979 The relative diffusion of a cloud of passive contaminant in incompressible turbulent flow. *J. Fluid Mech.* **91**, 337–355.

Cho, M. S. & Chung, M. K. 1997 Application of a Reynolds stress/heat flux model to the turbulent thermal dispersion behind a line heat source in a uniformly sheared flow. *Numer. Heat Transfer* A-*Applications* **32**, 715–732.

Christensen, K. T. & Adrian, R. J. 2001 Statistical evidence of hairpin vortex packets in wall turbulence. *J. Fluid Mech.* **431**, 433–443.

Chung, M. K., & Kyong, N. H. 1989 Measurement of turbulent dispersion behind a fine cylindrical heat source in a weakly sheared flow. *J. Fluid Mech.* **205**, 171–193.

Dupont, A., El Kabiri, M. & PAranthoen, P. 1985 Dispersion from elevated line source in a turbulent boundary layer. *Intl J. Heat Mass Transfer* **28**, 892–894.

Durbin, P. A. 1980 A stochastic model of two-particle dispersion and concentration fluctuations in homogeneous turbulence. *J. Fluid Mech.* **100**, 279–302.

El Kabiri, M., Paranthoen, P., Rosset, L. & Lecordier, J. C. 1998 Fluctuations de temperature et flux de chaleur en aval d'une source linéaire placée dans une couche limite turbulente. *Rev. Gén. Therm.* **37**, 181–194.

Fackrell, J. E. & Robins, A. G. 1982 Concentration fluctuations and fluxes in plumes from point source in a turbulent boundary layer. *J. Fluid Mech.* **117**, 1–26.

Holmes, P., Lumley, J. L. & Berkooz, G. 1996 *Turbulence, Coherent Structures, Dynamical Systems, and Symmetry* Cambridge University Press.

Hunt, J. C. R. 1985. Turbulent diffusion from sources in complex flows. *Annu. Rev. Fluid Mech.* **17**, 447–485.

Ilipoulos, I. & Hanratty, T. J. 1999 Turbulent dispersion in a non-homogenous field. *J. Fluid Mech.* **392**, 45–71.

Karnik, U. & Tavoularis, S. 1989 Measurements of heat diffusion from a continuous line source in a uniformly sheared turbulent flow. *J. Fluid Mech.* **202**, 233–261.

Khoo, B. C., Chew, Y. T. & Teo, C. J. 2000 On near-wall hot-wire measurements. *Exps. Fluids* **29**, 448–460.

Kim, K. C. & Adrian, R. J. 1999 Very large-scale motion in the outer layer. *Phys. Fluids* **11**, 417–422.

Kontomaris, K. & Hanratty, T. J. 1994 Effect of a molecular diffusivity on point source diffusion in the center of a numerically simulated turbulent channel flow. *Intl J. Heat Mass Transfer* **37**, 1817–1828.

Lavertu, R. A. 2002. Scalar dispersion in turbulent channel flow. MEng thesis, McGill University.

Legg, B. J., Raupach, M. R. & Coppin, P. A. 1986 Experiments on scalar dispersion within a model plant canopy Part III: An elevated line source. *Boundary-Layer Met.* **35**, 277–302.

Lemay, J. & Jean, Y. 2001. Constant current anemometer utilization guide. Université Laval, Québec, Canada.

Lemay, J. & Benaïssa, A. 2001 Improvement of cold-wire response for measurement of temperature dissipation, *Exps. Fluids* **31**, 347–356.

Lienhard, J. H. 1988 The decay of turbulence in thermally stratified flow. PhD dissertation, University of California at San Diego.

Liu, Z., Adrian, R. J. & Hanratty, T. J. 2001 Large-scale modes of turbulent channel flow: transport and structure. *J. Fluid Mech.* **448**, 53–80.

Livescu, D., Jaberi, F. A. & Madnia, C. K. 2000 Passive-scalar wake behind a line source in grid turbulence. *J. Fluid Mech.* **416**, 117–149.

Lyons, S. L. & Hanratty, T. J. 1991 Direct numerical simulation of passive heat transfer in a turbulent channel flow. *Intl J. Heat Mass Transfer* **34**, 1149–1161.

McLeod, M. S. 2000 On the design and testing of a high-aspect-ratio channel for turbulent flow measurements. BEng thesis, McGill University.

Mehta, R. D. 1977 The aerodynamic design of blower tunnels with wide-angle diffusers. *Prog. Aerospace Sci.* **18**, 59–120.

Mehta, R. D. & Bradshaw, P. 1979 Design rule for small low speed wind tunnels. *Aeronautical J.* Nov. 443–449.

Mydlarski, L. & Warhaft, Z. 1998 Passive scalar statistics in high-Péclet-number grid turbulence. *J. Fluid Mech.* **358**, 135–175.

Na, Y. & Hanratty, T. J. 2000 Limiting behavior of turbulent scalar transport close to a wall. *Intl J. Heat Mass Transfer* **43**, 1749–1758.

Papavassiliou, D. V. & Hanratty, T. J. 1997 Transport of a passive scalar in a turbulent channel flow. *Intl J. Heat Mass Transfer* **40**, 1303–1311.

Paranthoen, P., Fouari, A., Dupont, A. & Lecordier, J. C. 1988 Dispersion measurements in turbulent flows (boundary layer and plane jet). *Intl J. Heat Mass Transfer* **31**, 153–165.

Pope, S. B. 2000 *Turbulent Flows* Cambridge University Press.

Raupach, M. R. & Legg, B. J. 1983 Turbulent dispersion from an elevated line source: measurements of wind-concentration moments and budgets. *J. Fluid Mech.* **136**, 111–137.

Reshotko, E., Saric, W. S. & Nagib, H. M. 1997 Flow quality issues for large wind tunnels. *Proc. of the 35th Aerospace Sciences Meeting and Exhibit, Reno, AIAA Paper* 97-0225.

Robinson, S. K. 1991 Coherent motions in the turbulent boundary layer. *Annu. Rev. Fluid Mech.* **23**, 601–639.

Sawford, B. L. & Hunt, J. C. R. 1986 Effects of turbulence structure, molecular diffusion and source size on scalar fluctuations in homogeneous turbulence. *J. Fluid Mech.* **165**, 373–400.

Shah, D. A., Chambers, A. J. & Antonia, R. A. 1983 Reynolds number dependence of a fully developed turbulent duct flow. *Eighth Australian Fluid Mech. Conf. University of Newcastle.*

Shlien, D. J. & Corrsin, S. 1976 Dispersion measurements in a turbulent boundary layer. *Int. J. Heat Mass Transfer* **19**, 285–295.

Shraiman, B. I. & Siggia, E. D. 2000 Scalar turbulence. *Nature* **405**, 639–646

Sreenivasan, K. R. 1991 On local isotropy of passive scalars in turbulent shear flows. *Proc. R. Soc. Lond.* A **434**, 165–182.

Stapountzis, H., Sawford, B. L., Hunt, J. C. R. & Britter, R. E. 1986 Structure of the temperature field downwind of a line source in grid turbulence. *J. Fluid Mech.* **165**, 401–424.

Stapountzis, H. & Britter, R. E. 1987 Turbulent diffusion behind a heated line source in a nearly homogeneous turbulent shear flow. In *Proc. 6th Symp. on Turbulent Shear Flows, Toulouse* Springer.

Taylor, G. I. 1921 Diffusion by continuous movements. *Proc. Lond. Math. Soc.* A **20**, 196–212.

Taylor, G. I. 1935 Statistical theory of turbulence. IV-Diffusion in a turbulent air stream. *Proc. R. Soc. Lond.* A **151**, 465–478.

Taylor, G. I. 1953 Dispersion of soluble matter in solvent flowing slowly through a tube. *Proc. R. Soc. Lond.* A **219**, 186–203.

Taylor, G. I. 1954 The dispersion of matter in turbulent flow through a pipe. *Proc. R. Soc. Lond.* A **223**, 446–468.

Tennekes, H. & Lumley, J. L. 1972 *A First Course in Turbulence* MIT Press.

Thomson, D. J. 1990 A stochastic model for the motion of particle pairs in isotropic high-Reynolds-number turbulence, and its application to the problem of concentration variance. *J. Fluid Mech.* **210**, 113–153.

Tong, C. & Warhaft, Z. 1995 Passive scalar dispersion and mixing in a turbulent jet. *J. Fluid Mech.* **292**, 1–38.

Townsend, A. A. 1954 The diffusion behind a line source in homogeneous turbulence. *Proc. R. Soc. Lond.* A **224**, 487.

Uberoi, M. S. & Corrsin, S. 1953 Diffusion from a line source in isotropic turbulence. *NACA TN* 2710 (also *NACA Rep.* 1142).

Veeravalli, S. & Warhaft, Z. 1990 Thermal dispersion from a line source in the shearless turbulence mixing layer. *J. Fluid Mech.* **216**, 35–70.

Villermaux, E., Innocenti, C. & Duplat, J. 1998. Scalar fluctuation PDFs in transient turbulent mixing. *C. R. Acad. Sci. Ser. IIb: Mec. Phy. Chim. Astron.* **326**, 21–26.

Villermaux, E., Innocenti, C. & Duplat, J. 2001 Short circuits in the Corrsin–Obukhov cascade. *Phys. Fluids* **13**, 284–289.

Vincont, J. Y., Simoens, S., Ayrault, M. & Wallace, J. M. 2000 Passive scalar dispersion in a turbulent boundary layer from a line source at the wall and downstream of an obstacle. *J. Fluid Mech.* **424**, 127–167.

Vrieling, A. J. & Nieuwstadt, F. T. M. 2003 Turbulent dispersion from nearby point sources–interference of the concentration statistics. *Atmos. Environ* **37**, 4493–4506.

Wallace, J. M., Eckelmann, H. & Brodkey, R. S. 1972 The wall region in turbulent shear flow. *J. Fluid Mech.* **54**, 39–48.

Wang, Y. & Komori, S. 1999 Application of a second-moment closure model to simulate the turbulent dispersion from an elevated source. *Heat Mass Transfer* **34**, 429–436.

Warhaft, Z. 1984 The interference of thermal fields from line sources in grid turbulence. *J. Fluid Mech.* **144**, 363–387.

Warhaft, Z. 2000 Passive scalars in turbulent flows. *Annu. Rev. Fluid Mech.* **32**, 203–240.

Willmarth, W. W. & Lu, S. S. 1972 Structure of the Reynolds stress near the wall. *J. Fluid Mech.* **5**, 65–92.

Wilson, J. D., Flesch, T. K. & Swaters, G. E. 1993 Dispersion in sheared Gaussian homogeneous turbulence. *Boundary-Layer Met.* **62**, 281–290.

Wyngaard, J. C. 1968 Measurements of small-scale turbulence structure with hot wires. *J. Sci. Instr. Series 2* **1**, 1105–1108.

Wyngaard, J. C. 1971. Spatial resolution of a resistance wire temperature sensor. *Phys. Fluids* **14**, 2052–2054.

Zhukauskas, A. 1972 Heat transfer from tubes in cross flow. In *Advances in Heat Transfer*, vol. 8. Academic.